Estimating the neutron yield in a deuterium–tritium plasma with the JET neutron camera

Cite as: Rev. Sci. Instrum. 96, 063501 (2025); doi: 10.1063/5.0231639
Submitted: 1 August 2024 • Accepted: 28 April 2025 •
Published Online: 4 June 2025

Linus Hägg,[1,a)] Sean Conroy,[1] Göran Ericsson,[1] Zamir Ghani,[2] Luca Giacomelli,[3] Daniele Marocco,[4] Alberto Milocco,[5] Marco Riva,[4] Benjamin Vingren,[1] Gustav Robertson,[1] Jacob Eriksson,[1] Erik Andersson Sundén,[1] JET Contributors[b)] and Eurofusion Tokamak Exploitation Team[c)]

AFFILIATIONS

[1] Department of Physics and Astronomy, Uppsala University, SE-751 05 Uppsala, Sweden
[2] United Kingdom Atomic Energy Authority, Culham Science Centre, Abingdon, Oxon OX14 3DB, United Kingdom
[3] European Commission—Joint Research Centre, Via Enrico Fermi 2749, 21027 Ispra, VA, Italy
[4] Fusion and Technology for Nuclear Safety and Security Department, ENEA, C.R. Frascati, Via E. Fermi 45, I-00044 Frascati (Roma), Italy
[5] Physics Department "G. Occhialini," University of Milano–Bicocca University, Milano, Italy

[a)] **Author to whom correspondence should be addressed:** linus.hagg@physics.uu.se
[b)] See the author list of "Overview of JET results for optimising ITER operation" by J. Mailloux *et al.*, Nucl. Fusion **62**, 042026 (2022).
[c)] See the author list of E. Joffrin *et al.*, Nucl. Fusion (in press) (2024), https://doi.org/10.1088/1741-4326/ad2be4

ABSTRACT

The JET neutron camera is used to monitor a 2D profile of the neutron emission from the plasma, using 19 sightlines with plastic scintillators suited for measuring neutrons from the D + T → n + ^{4}He (DT) reaction. This paper describes an independent, first-principles physics method for estimating the volume integrated DT neutron yield with the neutron camera. This is performed for a selection of shots from the two recent DT campaigns at JET, the DTE2 and DTE3 JET campaigns. It covers the data reduction methods from a light yield calibration of the scintillators to treatment of pile-up, which is prevalent during high yield DT experiments. Several models of the camera geometry are used to account for scattering and transmission effects in the neutron transport. The neutron yield is estimated using models of the neutron emission profile, which are fitted to measurement data. The neutron yield estimates from this method are compared to corresponding estimates from the JET fission chambers. Our estimates with the neutron camera are on average 34% and 41% higher than the fission chamber estimates for DTE2 and DTE3, respectively. The reasons for the discrepancies between the two systems are presently unknown and prompt further investigation. In this paper, we detail the methods used to reach the neutron yield estimate from the neutron camera, along with their strengths, weaknesses, and potential points of failure. This method is an evolution of an earlier work that estimated the deuterium–deuterium neutron yield using similar methods.

I. INTRODUCTION

JET experiments rely on a great number of important diagnostics to monitor and manage the fusion plasma. Among these diagnostics, neutron measurements play a key role. The latest experimental deuterium–tritium (DT) campaigns at JET have been DTE2[1] and DTE3.[2] In the fusion reaction between deuterium and tritium in a tokamak plasma, neutrons are produced with an average energy of 14 MeV. Measurements of the DT neutron emission can, e.g., provide estimates of the volume integrated DT neutron yield, which is directly related to the fusion energy. Neutron measurements can also provide information about the plasma ion velocity distribution,[3–5] which in turn relates to the ion temperature,[6,7] ion densities,[8–11] the plasma rotation,[12] and the ratio of neutrons originating from thermal reactions compared to non-thermal reactions.[13,14]

This work uses measurement data from the JET neutron profile monitor,[15,16] commonly referred to as the JET neutron camera. An estimate of the DT neutron yield is derived from measurement data from the JET neutron camera and models describing the neutron emission from the fusion plasma, its transport to the neutron camera along with scatter in surrounding materials, and finally the detector response to the neutrons. Parameters in the neutron emission model are then adjusted in a fit until the simulated detector response matches the measurement data. The neutron yield can then be estimated from the best-fit neutron emission model.

The DT neutron yield estimates using camera data are compared to another estimate from a separate detector system, the JET fission chambers.[17,18] This is a continuation and an evolution of an earlier work that estimated the deuterium–deuterium (DD) neutron yield using a similar methodology.[19] We recommend the reader familiarize themselves with Ref. 19 before reading this work, as many of the systems and models are explained in more detail there. This work, however, uses another set of detectors in the JET neutron camera suited for DT measurements. It also includes an update to the data reduction codes to handle the significant increase in pile-up events due to the higher neutron rates in DT experiments compared to DD. Furthermore, it uses a more flexible neutron emission profile model, which is not dependent on any other detector systems at JET. A comparison is also made to the neutron emission profile provided by the code TRANSP.[12]

This paper covers the following areas: In Sec. II the JET neutron camera is described along with the method used for light yield calibration and how the measurement data are processed. Section III describes the models of the camera geometry and neutron transport, models of the neutron emission profile, and how the neutron yield is estimated. Section IV presents the resulting neutron yield estimates and features of the fitted neutron emission profiles. In Sec. V, we discuss the strengths and weaknesses of the methods used in this work.

II. NEUTRON CAMERA AND MEASUREMENTS

The JET neutron camera has 19 sightlines, also referred to as channels. A schematic of the detector system can be seen in Fig. 1, where the horizontal camera is comprised of channels 1–10 and the vertical camera of channels 11–19. All channels were used for the DTE2 campaign, but channels 13 and 18 were inactive during most of the DTE3 campaign. Each line of sight is equipped with an NE213 liquid scintillator for detecting DD neutrons (used in Ref. 19) and a BC418 (Bicron) plastic scintillator[20] for detecting DT neutrons. Gammas and neutrons interact with the BC418 scintillator material in various ways, resulting in scintillation light produced by the slowing down of particles such as electrons, protons, alpha particles, and carbon. The main contributors of scintillation light are electrons, due to gamma interactions, and protons, due to neutron interactions. We express this light yield in electron equivalent (ee) energy, in units of eVee, to relate the energy deposited from an incident neutron to that of a gamma ray. A photomultiplier tube connected to the scintillator[21] converts the scintillation light into voltage pulses, which are recorded as events in the data acquisition system. The integrated pulse area $Q[\mathrm{C}]$ of a voltage pulse is proportional to the deposited light yield $L[\mathrm{MeVee}]$, which is acquired through a light yield calibration.

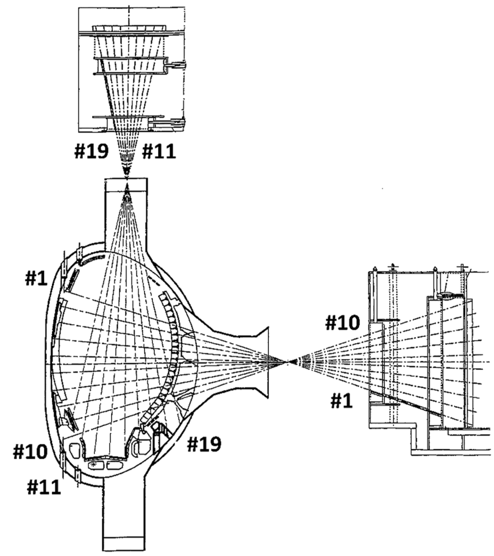

FIG. 1. Poloidal cross section of the JET neutron camera, adapted from JG96.200-3c in the JET Figure Database,[22] copyright by EFDA-JET. Channels 1–10 make up the horizontal camera, and channels 11–19 the vertical camera.

A. Light yield calibration

The integrated pulse area of an event is converted to light yield with a light yield calibration as

$$L = k \cdot Q, \tag{1}$$

where L is the light yield in MeVee, Q is the integrated pulse area in the digitizer amplitude unit of codes, and k is a calibration parameter.

As a plasma is subjected to Ohmic heating, i.e., in the absence of the auxiliary plasma heating methods neutral beam injection (NBI) and radio-frequency (RF) heating, the emitted neutron spectrum is well-known and well-suited for calibration purposes.[23] The calibration is performed using measurement data from time periods when the plasma is only subjected to Ohmic heating; this is hereafter referred to as thermal data. The neutron camera is equipped with ^{22}Na sources used to calibrate the NE213 liquid scintillators in DD measurements. However, using these to calibrate the Bicrons would involve a hefty extrapolation to the higher energies in DT measurements. For this reason, we use thermal data instead to calibrate the neutron camera for DT measurements.

The light yield calibration is divided into a primary and a secondary calibration, which use two different methods. The central channels are fully calibrated using thermal data in the primary calibration, as described in Secs. II A 1 and II A 2. This method can only be used for the central channels, since the edge channels lack a sufficient amount of thermal data. The secondary calibration is used to calibrate the edge channels (see Sec. II A 3). The k parameters are estimated for the edge channels using data from shots with both ohmic and neutral beam injection heating in order to acquire enough counts for the calibration fit.

The primary calibration uses thermal data from hundreds of JET shots from the DTE2 and DTE3 campaigns. Due to the high load exerted on the detector system by the intense neutron fluxes during these campaigns, detector gain drift must be considered. Ideally, a shot should be calibrated using thermal data collected from that same or a neighboring shot. However, to acquire a sufficient number of counts for the analysis (even for the central channels), we require a sum of thermal data from many shots. For the JET DTE2 campaign, we use thermal data from 530 shots in the range 99440–99969. These are divided into five overlapping groups, which allows for a linear approximation of the gain drift throughout the campaign. Group 1 covers shots 99440–99596, group 2 covers shots 99528–99703, group 3 covers shots 99597–99792, group 4 covers shots 99704–99880, and group 5 covers shots 99793–99969. For the JET DTE3 campaign, we use thermal data from 846 shots in the range 103900–105499. In this case, the number of counts was too few to divide the thermal data into smaller groups for a linear approximation. Instead, the complete sum is used, which averages the gain drift over the whole shot group for the DTE3 calibration.

1. Model

A model of the thermal neutron pulse height spectrum (PHS) is used in the primary calibration. The neutron energy spectrum from a thermal DT plasma can be described as a Gaussian with the full width at half maximum expressed as

$$FWHM_a = \sqrt{T_{\rm i}}(a_1 + T_{\rm i}(a_2 + T_{\rm i}(a_3 + T_{\rm i} * a_4))), \tag{2}$$

where T_i is the ion temperature set to a typical ion temperature of 4 keV,[24] and the coefficients a_1, a_2, a_3, and a_4 are calculated by the Van Belle and Sadler FPS (Fusion Product Spectra) code[25] (see Table I). This results in a full width at half maximum value of $FWHM_a = 355$, which is nearly identical to the value obtained by Ballabio *et al.* in Ref. 26. The Gaussian is centered on $14\,028 + E_{\rm shift}$ keV with the energy shift

$$E_{\rm shift} = a_5 + T_{\rm i}(a_6 + T_{\rm i}(a_7 + T_{\rm i} * a_8)), \tag{3}$$

where the coefficients a_5, a_6, a_7, and a_8 are also given by the Van Belle and Sadler FPS code (see Table II). This results in an energy shift of $E_{\rm shift} = 18.5$ keV, which is nearly identical to the value obtained by Ballabio *et al.* in Ref. 26.

TABLE I. Coefficients used in Eq. (2) for a thermal DT plasma.

$T_{\rm i}$ (keV)	a_1	a_2	a_3	a_4
4	177.232	0.091 474	-4.9222×10^{-3}	1.0108×10^{-4}

TABLE II. Coefficients used in Eq. (3) for a thermal DT plasma.

$T_{\rm i}$ (keV)	a_5	a_6	a_7	a_8
4	1.856 05	4.826 73	−0.181 232	3.2483×10^{-3}

The model of the thermal neutron spectrum is folded with the system response matrix (see Sec. III B 4), which results in a PHS with neutron rate over light yield. A Gaussian broadening is also applied on the model PHS with a full width at half maximum described by

$$FWHM_b = b \cdot \sqrt{L}, \tag{4}$$

where b is a calibration parameter and L is the light yield.

2. Primary calibration

The modeled thermal neutron energy spectrum from Eqs. (2) and (3) is folded with the system response matrix and compared to the measured thermal neutron PHS, an example of which is shown in Fig. 3. A goodness-of-fit is calculated using the CSTAT test statistic,[27] which is defined as

$$CSTAT = 2\sum_i (e_i - n_i \ln e_i), \tag{5}$$

where e_i are binned model values and n_i are binned measurement values for channel i. Each channel has a set of calibration parameters, k_i and b_i. The measurement values n_i are expressed in light yield using k_i in Eq. (1). The Gaussian broadening on the model values e_i is adjusted with b_i based on Eq. (4). The calibration is performed by varying the parameters k_i and b_i to minimize CSTAT, as calculated by Eq. (5). Note that the light yield calibration only requires k_i, but the parameter b_i is later used with the system response matrix (see Sec. III B 4).

For the thermal data used in this work, only the central detector channels have a sufficient number of counts to perform this fit reliably. For this reason, the primary calibration is performed only for channels 4, 5, 6, 14, 15, and 16. The remaining channels are calibrated in the secondary calibration (see Sec. II A 3).

For DTE2, this calibration is performed for each of the five summed shot groups. The calibration fit finds individual k-parameters for each channel in each group but a common b-parameter for each channel that is used in all groups. We use a linear approximation as

$$k_i = \alpha_i \cdot N_{\rm shot} + \beta_i, \tag{6}$$

where k_i is the interpolated calibration coefficient, α and β are the linear parameters, and $N_{\rm shot}$ is the JET shot number. For this approximation, we have used the middle-shot in each shot group. It is not known whether the gain drift has degraded steadily over time or if the degradation primarily happens under heavy loads during high neutron fluxes. As a simplification and a compromise, we choose to interpolate over shot numbers. The fitted parameters and the linear parameters between them are shown in Table III; examples of the linear approximations for channels 14 and 15 are shown in Fig. 2.

The uncertainties in the calibration factors result in large uncertainties in the linear parameters α_i and β_i (see Table IV). As a result, the impact of gain drift cannot be reliably gauged from these linear approximations. Some channels, such as 14, indicate a gain drift over the campaign. While other channels, such as 15, do not show the same kind of indication. The shaded area in Fig. 2 marks the 1-sigma uncertainty region of k_i for the linear approximation.

TABLE III. Parameter values with absolute statistical uncertainties in parentheses from the DTE2 primary calibration.

	Group 1	Group 2	Group 3	Group 4	Group 5	
Channel	k	k	k	k	k	b
4	0.48(0.04)	0.47(0.05)	0.50(0.01)	0.50(0.03)	0.50(0.02)	0.43(0.40)
5	0.41(0.04)	0.41(0.02)	0.42(0.03)	0.43(0.03)	0.43(0.03)	0.54(0.39)
6	0.54(0.03)	0.54(0.02)	0.55(0.02)	0.54(0.02)	0.54(0.02)	0.27(0.43)
14	0.36(0.02)	0.36(0.03)	0.38(0.02)	0.38(0.03)	0.39(0.02)	0.67(0.70)
15	0.43(0.02)	0.40(0.02)	0.44(0.01)	0.43(0.02)	0.42(0.01)	0.33(0.27)
16	0.37(0.02)	0.37(0.03)	0.38(0.02)	0.39(0.03)	0.38(0.02)	0.42(0.41)

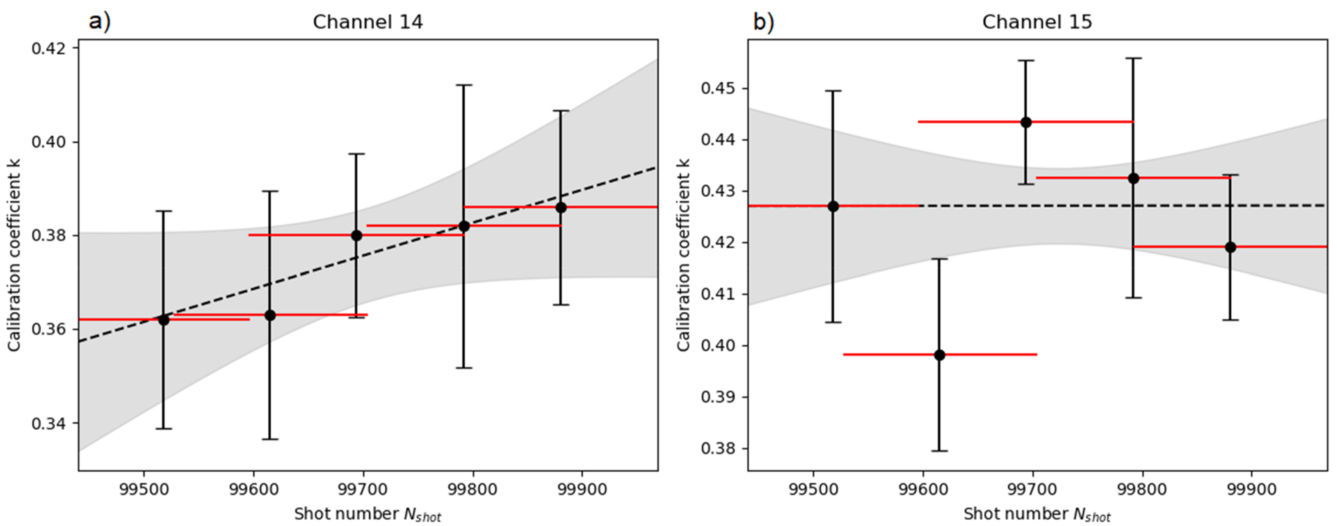

FIG. 2. Calibration factor k calculated for the five datasets of the DTE2 campaign. The dashed black line is a linear approximation of the gain drift during DTE2 for channel 14 (a) and channel 15 (b). The shaded area marks the 1-sigma uncertainty region for the linear approximation. The red lines indicate the span of each shot group, as opposed to the vertical black lines, which show the uncertainty of the calibration method for each shot group.

For DTE3, the fit is performed for the single group of summed thermal data. The fitted parameters are shown in Table V, and an example of a completed fit for channel 15 is shown in Fig. 3. DTE2 and DTE3 suffer similarly sized calibration uncertainties; both of these are propagated through the analysis into an uncertainty of the neutron yield estimate. For both DTE2 and DTE3, the uncertainties of the parameter b are especially high. However, b is a measure of the detector resolution, which has a very low impact on the detector efficiency. Since the aim of the method is to estimate the neutron yield, it is not very sensitive to even large uncertainties in b.

TABLE IV. Linear approximation parameters with absolute statistical uncertainties in parentheses from the DTE2 primary calibration.

Channel	α	β
4	$5.4(8.8) \times 10^{-5}$	−4.9(8.8)
5	$4.2(11.7) \times 10^{-5}$	−3.8(11.7)
6	$4.5(82.1) \times 10^{-6}$	−0.09(8.2)
14	$7.0(8.0) \times 10^{-5}$	−6.6(8.0)
15	$1.9(6245.0) \times 10^{-7}$	−0.41(6.23)
16	$3.8(7.4) \times 10^{-5}$	−3.4(7.4)

TABLE V. Parameter values with absolute statistical uncertainties in parentheses from the DTE3 primary calibration.

Channel	k	b
4	0.54(0.04)	0.53(0.30)
5	0.46(0.04)	0.62(0.60)
6	0.59(0.04)	0.44(0.33)
14	0.41(0.05)	0.49(0.39)
15	0.47(0.01)	0.45(0.19)
16	0.42(0.05)	0.64(0.61)

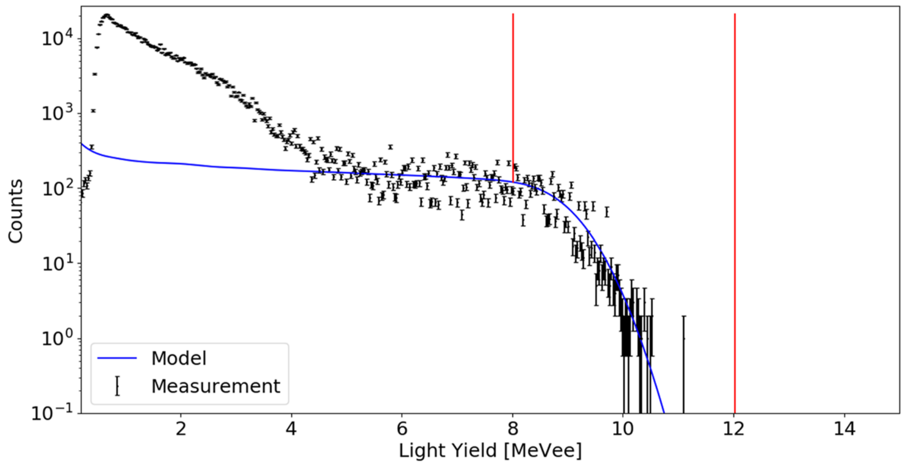

FIG. 3. Pulse height histogram of thermal data for in-camera channel 15 with the best-fit model. The red vertical lines denote the region in which CSTAT is calculated. The discrepancy between the model and measurements for light yields lower than 5 MeVee is due to gamma-induced events, which are not included in the model.

3. Secondary calibration

Despite summing many thermal shots, few channels have a sufficient number of counts to reliably perform the primary calibration. As can be deduced from Fig. 1, channels 1–3, 7–13, and 17–19 view the low ion density and temperature region of the plasma, resulting in an order of magnitude lower count rate compared to the channels with sightlines closer to the plasma core. For these channels, we perform a secondary calibration to evaluate their k parameters in a different CSTAT minimization than in the primary calibration. Instead of using thermal data, we use data from a small sum of shots with both ohmic and neutral beam injection heating. The PHS of each edge channel is compared to the PHS of channel 15, which is already calibrated with the primary calibration. The k parameter for channel 15 is scaled by a parameter c, which is varied during the fit. The k-values of the edge channels are then estimated as

$$k_i = k_{15} \cdot c_i, \tag{7}$$

where k_i is the calibration parameter and c is a stretch factor for detector channel i. For DTE2, we perform this fit for each of the five groups (see Table VI), but for DTE3 we only obtain a single set

TABLE VI. Stretch factors for DTE2 with absolute statistical uncertainties in parentheses. The c-values are relative to channel 15, i.e., $c_{15} = 1$.

	Group 1	Group 2	Group 3	Group 4	Group 5
Channel	c	c	c	c	c
1	1.183(0.028)	1.185(0.015)	1.185(0.017)	1.193(0.023)	1.179(0.030)
2	1.027(0.023)	1.027(0.013)	1.027(0.014)	1.022(0.019)	1.027(0.024)
3	0.990(0.023)	0.993(0.012)	0.994(0.014)	0.999(0.019)	0.998(0.023)
4	1.119(0.025)	1.119(0.014)	1.119(0.016)	1.119(0.021)	1.139(0.026)
5	0.942(0.021)	0.945(0.011)	0.943(0.014)	0.955(0.018)	0.953(0.022)
6	1.311(0.031)	1.279(0.016)	1.279(0.018)	1.266(0.024)	1.247(0.030)
7	1.312(0.034)	1.317(0.017)	1.316(0.020)	1.296(0.025)	1.317(0.030)
8	1.135(0.028)	1.139(0.015)	1.139(0.017)	1.160(0.022)	1.144(0.029)
9	1.072(0.029)	1.065(0.015)	1.061(0.016)	1.079(0.021)	1.067(0.029)
10	1.011(0.034)	1.002(0.018)	0.998(0.018)	1.001(0.021)	1.001(0.030)
11	0.951(0.023)	0.949(0.012)	0.949(0.014)	0.952(0.018)	0.943(0.023)
12	0.981(0.023)	0.984(0.012)	0.981(0.014)	0.990(0.019)	0.985(0.024)
13	1.092(0.025)	1.092(0.013)	1.092(0.015)	1.089(0.020)	1.085(0.025)
14	0.835(0.019)	0.850(0.010)	0.851(0.013)	0.873(0.016)	0.886(0.020)
15	1.000(0.023)	1.000(0.012)	1.000(0.014)	1.000(0.019)	1.000(0.023)
16	0.871(0.020)	0.872(0.011)	0.872(0.012)	0.875(0.016)	0.875(0.020)
17	1.131(0.026)	1.144(0.014)	1.150(0.017)	1.158(0.021)	1.177(0.027)
18	0.976(0.022)	0.965(0.012)	0.965(0.014)	0.975(0.018)	0.961(0.023)
19	1.012(0.025)	1.020(0.013)	1.020(0.015)	1.032(0.019)	1.016(0.025)

TABLE VII. Stretch factors and final calibration factors for DTE3 with absolute statistical uncertainties in parentheses.

Channel	c
1	1.183(0.011)
2	1.010(0.005)
3	1.005(0.003)
4	1.119(0.003)
5	0.955(0.003)
6	1.267(0.006)
7	1.305(0.017)
8	1.101(0.009)
9	1.022(0.012)
10	0.968(0.020)
11	0.928(0.008)
12	0.948(0.006)
13	N/A
14	0.869(0.002)
15	1.000(0.003)
16	0.845(0.002)
17	1.190(0.006)
18	N/A
19	0.983(0.008)

of stretch factors (see Table VII). The stretch factors are relative to channel 15, meaning $c_{15} = 1$. With Eq. (7), we can obtain the k-values for the edge channels, and in the case of DTE2, perform a linear approximation. The final k-values and linear parameters are listed in Table VIII. Note that channels 13 and 18 were not operational for the DTE3 shots used in this work.

Because the secondary calibration does not yield b-values, the edge channels use an average of the values from the primary calibration: $b = 0.445$ for DTE2 and $b = 0.497$ for DTE3.

B. Light yield threshold

Unlike with the NE213 scintillators used in Ref. 19, the pulse shapes from a BC418 scintillator cannot be used to distinguish whether a pulse originated from a gamma or a neutron. Instead, the neutron events are, to a large extent, separated from gamma events using a light yield threshold set at 6 MeVee (approximately corresponding to a full energy deposition from a 10 MeV neutron). Events above this threshold are dominated by DT neutrons; this excludes a vast majority of gamma events as well as neutrons from DD reactions. The light yield threshold was selected to be in between both the low light yield region (around 0–5 MeVee in Fig. 3), where gammas are prevalent, and the high light yield edge (approximately above 8 MeVee in Fig. 3), which is strongly affected by detector resolution broadening.

C. Pile-up

Pile-up is a generally unwanted feature of data collection where multiple events arrive at the detection system at the same time. This leads to voltage pulses partially or fully overlapping, which makes it difficult or impossible to distinguish their individual pulse heights. Due to the high neutron rates in DT experiments, a method has been developed to correct for pile-up events. All pulses that are recorded

TABLE VIII. Final calibration coefficients and linear approximation coefficients with absolute statistical uncertainties in parentheses.

		DTE2		DTE3
Channel	Calibration	α	β	k
1	Secondary	$-2.27(6.3) \times 10^{-6}$	0.73(7.63)	0.56(0.02)
2	Secondary	$-1.8(6.4) \times 10^{-5}$	2.2(6.4)	0.48(0.01)
3	Secondary	$-7.1(62.5) \times 10^{-6}$	1.1(6.2)	0.45(0.01)
4	Primary	$5.4(8.8) \times 10^{-5}$	−4.9(8.8)	0.54(0.04)
5	Primary	$4.2(11.7) \times 10^{-5}$	−3.8(11.6)	0.46(0.04)
6	Primary	$4.5(82.2) \times 10^{-6}$	0.09(8.20)	0.59(0.04)
7	Secondary	$-2.4(8.9) \times 10^{-5}$	3.0(8.9)	0.62(0.02)
8	Secondary	$-2.6(75.7) \times 10^{-6}$	10.74(7.54)	0.52(0.02)
9	Secondary	$-8.5(74.0) \times 10^{-6}$	1.3(7.4)	0.48(0.01)
10	Secondary	$-8.5(82.1) \times 10^{-6}$	1.3(8.2)	0.46(0.01)
11	Secondary	$-2.2(6.3) \times 10^{-5}$	2.6(6.2)	0.44(0.01)
12	Secondary	$-1.3(6.3) \times 10^{-5}$	1.7(6.3)	0.45(0.01)
13	Secondary	$-2.9(6.8) \times 10^{-5}$	3.4(6.8)	N/A
14	Primary	$7.0(8.0) \times 10^{-5}$	−6.6(8.0)	0.41(0.05)
15	Primary	$1.8(624.7) \times 10^{-7}$	0.41(6.23)	0.47(0.01)
16	Primary	$3.8(7.4) \times 10^{-5}$	−3.4(7.4)	0.42(0.05)
17	Secondary	$3.2(7.2) \times 10^{-5}$	−2.7(7.2)	0.56(0.02)
18	Secondary	$-2.3(6.1) \times 10^{-5}$	2.7(6.1)	N/A
19	Secondary	$-1.3(6.6) \times 10^{-5}$	1.8(6.6)	0.46(0.01)

within 100 ns of one another are classified as pile-up events. The classification code tags all events as pile-up or non-pile-up accordingly. The code is unable to identify pile-up events where two (or more) pulses overlap in such a way that only one peak can be distinguished; that type of pile-up is not accounted for. The integrated pulse areas of pile-up events are compromised due to the close vicinity of neighboring pulses. We account for this issue by calculating the ratio of non-pile-up events above and below the light yield threshold. Since both pile-up events and non-pile-up events originate from the same neutron energy distribution, both event types should have the same ratio of events above and below the light yield threshold. Therefore, the non-pile-up events above the light yield threshold are tallied, while the pile-up events are estimated using this ratio. For the highest rate shots used in this work, the measurement data can contain up to 68% pile-up events (channel 15, shot 104522 in the time interval 10.0–10.5 s). Shots with midrange rates can have around 29% pile-up events (channel 15, shot 104602 in the time interval 11.7–12.2 s), while low rate shots can have a negligible 0.6% of pile-up events (channel 15, shot 99716 in the time interval 13.0–13.5 s).

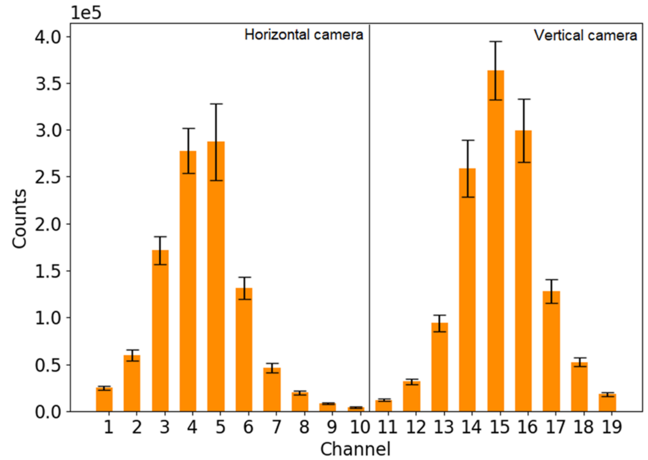

FIG. 5. Measured neutron count profile of JET shot 99950 in the time interval 10.0–10.5 s. The error bars are derived from statistical and light yield calibration uncertainties, as detailed in Sec. II A; however, the error is dominated by the calibration uncertainties.

D. Measured neutron counts

The recorded events in each detector channel are light yield calibrated (see Sec. II A) and then displayed in a PHS along with our chosen light yield threshold (see Fig. 4). Detector gain drifts will affect the number of counts above that threshold. Long-term gain drifts are accounted for as far as the uncertainties allow in the DTE2 measurement data as described in Sec. II A 2. The impact of short-term gain drifts is not accounted for but is further discussed in Sec. V A.

By summing events above the light yield threshold (see Sec. II B), while accounting for pile-up effects (see Sec. II C), we can describe the measured neutron count profile (see Fig. 5). The uncertainty of the light yield calibration is propagated to the uncertainties in the neutron count profile for each channel, as exemplified in Fig. 5.

III. MODELS AND SIMULATIONS

A. Neutron emissivity profile

This work mainly uses a simplified model describing the neutron emissivity from a poloidal slice of the plasma. The emission s is described by a two-dimensional Gaussian centered on an arbitrary point (R_0, Z_0), expressed as

$$s = r_n \cdot e^{-\left(\frac{(R-R_0)^2}{2\sigma_R^2}+\frac{(Z-Z_0)^2}{2\sigma_Z^2}\right)}, \tag{8}$$

where R is the major radius, Z is the height above the torus midplane, r_n is a scale factor, and σ_R and σ_Z are the standard deviations in the R- and Z-directions, respectively. Compared to the model used in our earlier work (Ref. 19), this model does not use estimates of the plasma magnetic flux surfaces. Consequently, the use of this model

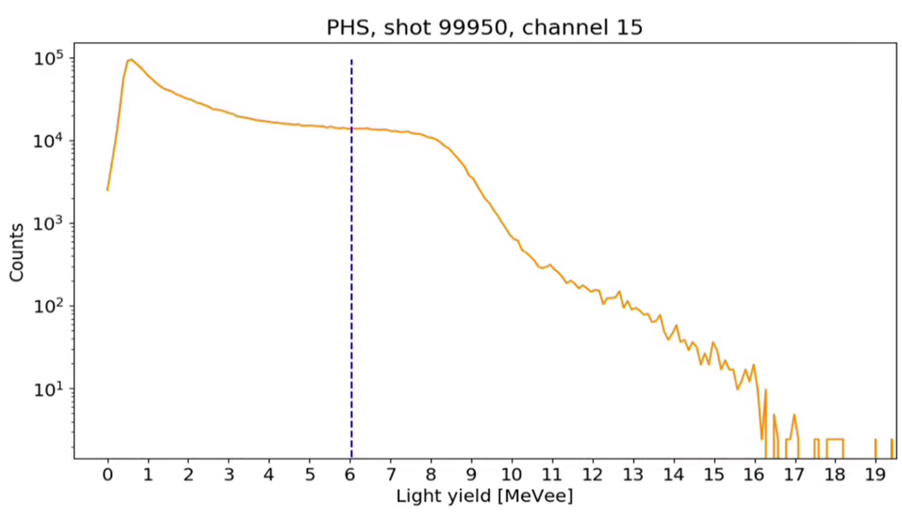

FIG. 4. Pulse Height Spectrum (PHS) of JET shot 99950 channel 15 in the time interval 10.0–10.5 s. The blue dashed line shows the light yield threshold at 6 MeVee.

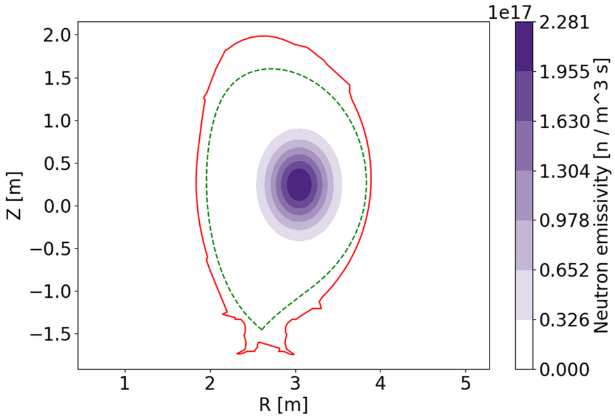

FIG. 6. Gaussian neutron emissivity profile model for JET shot 99950 in the time interval 10.0–10.5 s. The model parameters are $\sigma_R = 0.25$, $\sigma_Z = 0.33$, $R_0 = 3.05$, and $Z_0 = 0.24$. The dashed green outline indicates the last closed flux surface, while the solid red line shows the torus walls.

is not reliant on any measurement diagnostics other than the neutron camera. The use of separate widths in the R- and Z-directions allows the model to better describe neutron emissivity profiles that are not constant on each flux surface (e.g., due to the use of NBI or RF heating[28]). An example of the model is shown in Fig. 6.

The Gaussian model primarily describes the neutron emission from passing thermal–thermal and beam–thermal reactions. It does not have a component describing neutron emission from trapped beam–thermal reactions, which are expected to have an asymmetric non-Gaussian shape. Ronchi *et al.*[29] describes a parametric neutron emissivity profile model that includes the trapped elements along with a contribution from RF heating. This model demonstrated success using neural networks to describe the emission of certain JET shots. Ronchi's model is not used in this work, but it is a possible contender for future iterations of this method. The Gaussian model is relatively simple, but since the aim is to estimate the volume integrated neutron yield, a detailed shape is not crucial. To investigate the validity of this claim, we also performed an initial comparison with a more detailed neutron emission profile model from the plasma transport code TRANSP.[12] This model is not detailed in this work, but the results are discussed in Sec. V C.

A variant of the Gaussian model is also used, where the center of the Gaussian (R_0, Z_0) is fixed and determined using the Equilibrium Fitting code EFIT++/JEC2020.[30] We refer to this as the fixed Gaussian model.

B. Camera models

The simulated neutrons are divided into three categories: direct, in-scatter, and backscatter neutrons. Direct neutrons travel from the fusion plasma to the detectors without scattering in the collimator or in any other surrounding structure. In-scatter neutrons scatter against materials near the detectors before they are detected. Backscatter neutrons, on the other hand, scatter against the torus back wall[31] before reaching the detector.

In order to simulate neutrons from all categories, three different models are used. First, an optical model called LINE2.1 is used with the neutron emission profile model to simulate the direct neutron rate on each detector (see Sec. III B 1). Second, an MCNP (Monte Carlo N-Particle Transport) model, called the detector system model, which is a more detailed model of the channel 15 detector, collimator, and surrounding material, see Fig. 8. The detector system model is used to simulate the in-scatter neutrons and the detector light yield in order to construct a system response matrix (see Secs. III B 2–III B 4). Third, an MCNP model of the whole neutron camera and the JET torus wall, henceforth referred to as the JET model, is used to simulate the backscatter neutron spectrum for each channel (see Sec. III B 5).

The LINE2.1 model, the JET model, and the detector system model have a few notable differences compared to our earlier work (Ref. 19). In all models, the neutrons are tallied at the BC418 plastic scintillators (which are used to detect DT neutrons) rather than at the NE213 liquid scintillators (which are used to detect DD neutrons, as was performed in Ref. 19). All models use the narrower 10 mm diameter setting for the rotatable collimator, as intended for DT operation. The detector system model uses the BC418 light yield function described in Sec. III B 3. Finally, the neutron source in the detector system model illuminates more of the collimator compared to the modeling performed in Ref. 19. This is to account for transmission through the rotatable steel collimator, which is more important for the higher energy DT neutrons compared to the DD neutrons studied in Ref. 19.

1. Optical model

In the LINE2.1 model, the tokamak volume is divided into voxels. From each voxel, the model simulates isotropic neutron emission and calculates the probability of a neutron reaching the detector in each channel. All materials are considered to be perfect absorbers, meaning that only direct neutrons are accepted. A poloidal projection of the probability scaled with the voxel volume is shown in Fig. 7 together with the JET first wall.

2. Detector system model

The detector system model details detector channel 15 with its collimator, the surrounding concrete, and the detector box containing the scintillators, photomultiplier tubes, and the magnetic shielding. The model and its dimensions are found in Fig. 8.

For the MCNP settings used in the detector system model, we simulate both neutrons and protons. Specifically, the simulation considers the elastic and inelastic scattering of protons and neutrons and the slowing down of protons. Notably, the $^{12}C(n, 3\alpha)$ reaction is not included in this simulation. Most of the in-scatter neutrons have energies close to those of the direct neutrons. The energy spectrum for in-scattered neutrons in this model is shown in Fig. 9.

3. Light yield function

The light-yield generation in the Bicron detectors is broadly described by a function measured by Adams,[32] which was produced using BC418 scintillators similar to those in the neutron camera. Adams has produced light yield functions for both the NE213 and BC418 scintillators, the former of which was used in Ref. 19.

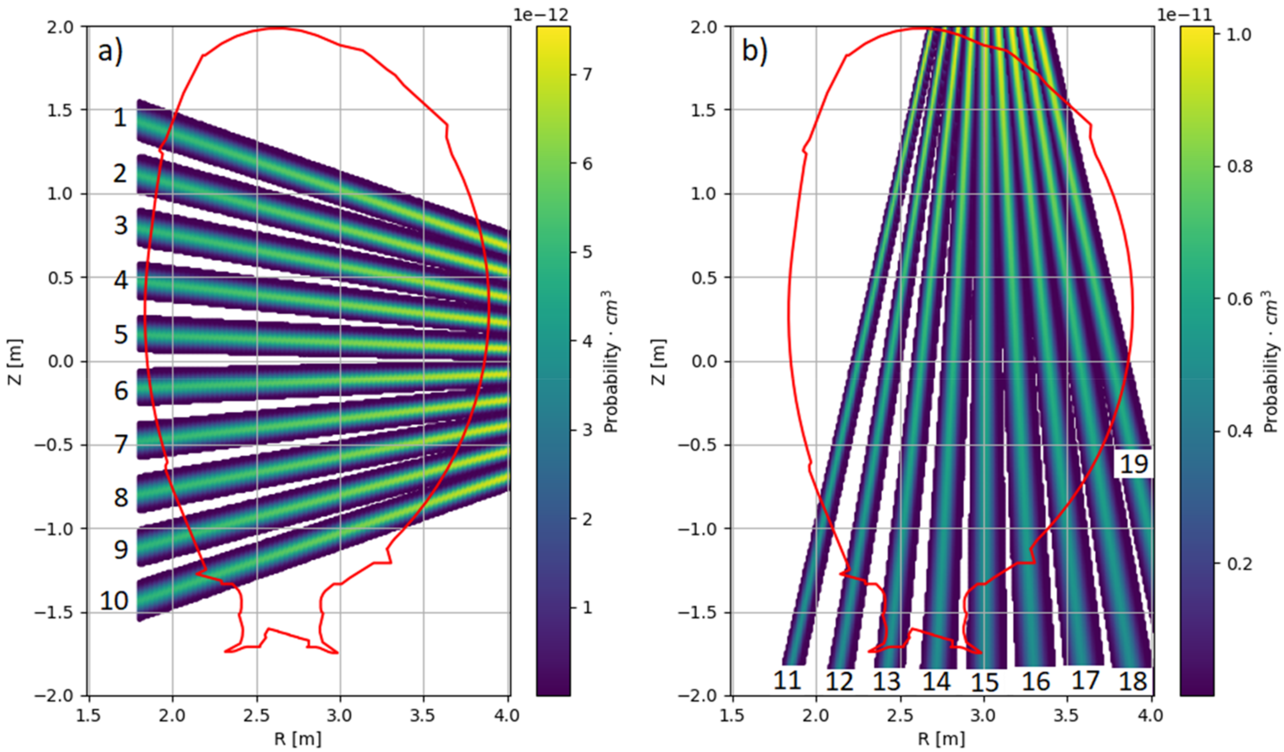

FIG. 7. Poloidal projection of the LINE2.1 probability for each channel in relation to the first wall. This represents the visibility of the plasma for the horizontal (a) and vertical (b) camera channels. Reproduced with permission from Hägg *et al*., Rev. Sci. Instrum. **94**, 073502 (2023). Copyright 2023 AIP Publishing.

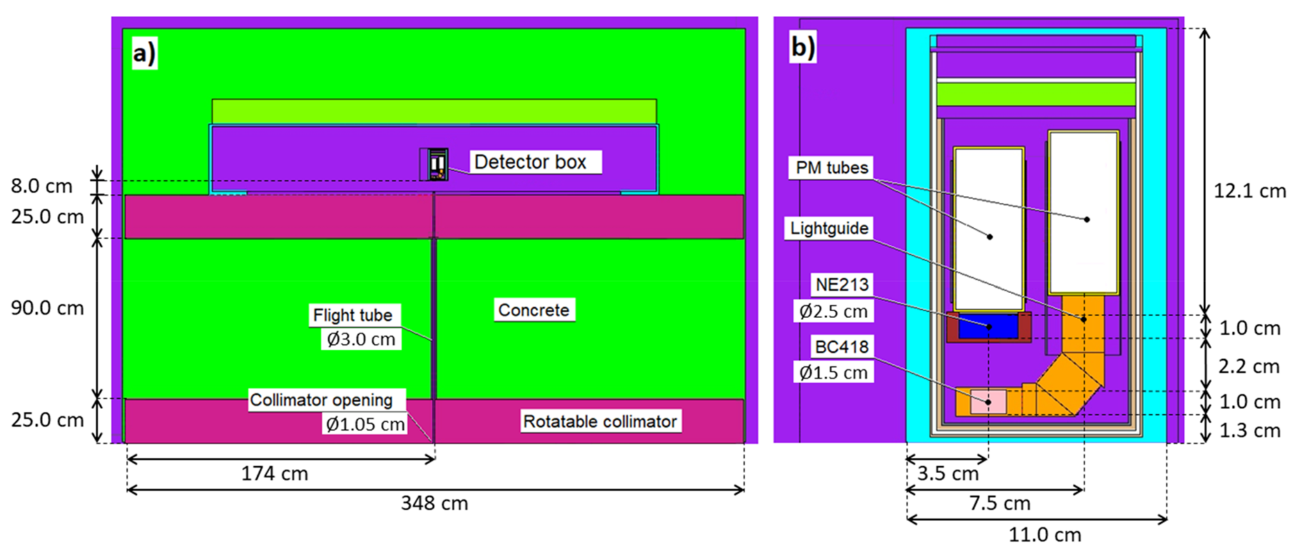

FIG. 8. MCNP detector system model. (a) Shows a cross section of the channel 15 collimator and its detector box. (b) shows a close-up of the detector box containing the NE213 and BC418 scintillator detectors. The detector box model is based on the illustration JG95.166-1c in the JET Figure Database,[22] copyright by EFDA-JET (see Appendix B). The light green areas in (a) are concrete, the magenta areas with the rotatable collimators are steel, and the purple areas are air. Reproduced with permission from Hägg *et al*., Rev. Sci. Instrum. **94**, 073502 (2023). Copyright 2023 AIP Publishing.

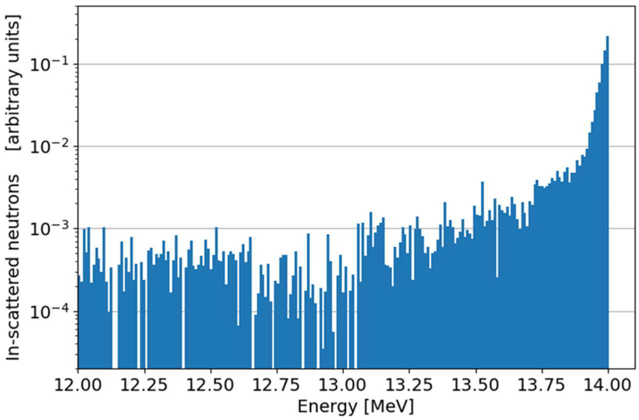

FIG. 9. Neutron energy spectrum for in-scattered neutrons in the MCNP detector system model for a monoenergetic 14 MeV neutron source.

The Adams light yield function for Bicron detectors is given over three energy intervals as

$$L = \begin{cases} x_1 + y_1 \cdot E_p + z_1 \cdot E_p^2 + w_1 \cdot E_p^3 : 0 \le E_p \le 5.425 \text{ MeV}, \\ x_2 + y_2 \cdot E_p + z_2 \cdot E_p^2 + w_2 \cdot E_p^3 : 5.425 < E_p \le 15.525 \text{ MeV}, \\ x_3 + y_3 \cdot E_p + z_3 \cdot E_p^2 + w_3 \cdot E_p^3 : 15.525 < E_p \le 18.93 \text{ MeV}, \end{cases} \tag{9}$$

where L is the light yield, E_p is the proton energy, and the other coefficients are listed in Table IX.

The detectors in the 19 camera channels have individual light yield characteristics. The Adams light yield function alone cannot accurately describe all these variations. However, it is used in the light yield calibration through the system response matrix. This approach allows each detector channel to be calibrated based on the Adams function, with individual k-values [see Eq. (7)] accounting for differences in light yield characteristics. As a result, the Adams light yield function can be used as a basis in the models to represent all detector channels.

4. System response matrix

The detector system model and the Adams light yield function are used to construct a system response matrix. This matrix is used to calculate the light yield spectrum for each detector for a given neutron emission spectrum from the fusion plasma. A corresponding matrix is also constructed in Ref. 19 using the same methodology as described below.

The detector system model is used in two separate MCNP simulations. In Simulation 1, we calculate the neutron current N into the detector while excluding neutrons from in-scatter and transmission through materials near the detector. This setup imitates the optical LINE2.1 model, where we only consider neutrons that reach the detector directly. In Simulation 2, we calculate the event rate in the detector while including events caused by neutrons from in-scatter and transmission through materials near the detector. We also use the Adams light yield function in Simulation 2 to calculate the associated light yield spectrum S. Simulation 1 and 2 both employ a monoenergetic neutron source at the collimator opening closest to the plasma. The ratio S/N describes the increase in the neutron rate (for different light yield bins) at the detector when in-scatter and transmission are accounted for compared to the purely optical case with the LINE2.1 model. The system response matrix is built through repeated simulations with monoenergetic neutron sources ranging between 11.2 and 17.1 MeV, in steps of 0.05 MeV. To emulate the detector resolution, we also apply a Gaussian broadening along the energy axis of the matrix using the light yield calibration parameter b for each respective channel (see Sec. II A 2).

Direct and in-scattered neutrons from a DT plasma are expected to have energies close to 14 MeV. As a simplification, we assume the plasma emits only monoenergetic 14 MeV neutrons. The row in the system response matrix corresponding to the simulated 14 MeV neutrons is summed above the light yield threshold of 6 MeVee, yielding an efficiency factor f_i for channel i. The efficiency factors are listed in Table X. The application of individual broadening values only changes the efficiency values on a percent level. The individual light yield calibrations for DTE2 and DTE3 also come with marginal differences due to broadening in their respective efficiency factors. By applying the efficiency factor to the simulated direct neutron rate, we estimate the neutron count rate in each channel while accounting for in-scatter and transmission.

TABLE IX. Coefficients used in Eq. (9).

i	x_i	y_i	z_i	w_i
1	0.0	0.0932	0.1014	−0.0068
2	−0.1393	0.2532	0.0472	−0.0014
3	−14.4633	3.8536	−0.2344	0.0057

TABLE X. Efficiency factors for all channels with absolute statistical uncertainties in parentheses.

Channel	DTE2 efficiency factor f	DTE3 efficiency factor f
1	$9.05(0.05) \times 10^{-3}$	$9.05(0.05) \times 10^{-3}$
2	$9.05(0.05) \times 10^{-3}$	$9.05(0.05) \times 10^{-3}$
3	$9.05(0.05) \times 10^{-3}$	$9.08(0.05) \times 10^{-3}$
4	$9.04(0.05) \times 10^{-3}$	$9.05(0.05) \times 10^{-3}$
5	$9.04(0.05) \times 10^{-3}$	$9.03(0.04) \times 10^{-3}$
6	$9.08(0.05) \times 10^{-3}$	$9.06(0.05) \times 10^{-3}$
7	$9.05(0.05) \times 10^{-3}$	$9.05(0.05) \times 10^{-3}$
8	$9.05(0.05) \times 10^{-3}$	$9.05(0.05) \times 10^{-3}$
9	$9.05(0.05) \times 10^{-3}$	$9.05(0.05) \times 10^{-3}$
10	$9.05(0.05) \times 10^{-3}$	$9.05(0.05) \times 10^{-3}$
11	$9.05(0.05) \times 10^{-3}$	$9.05(0.05) \times 10^{-3}$
12	$9.05(0.05) \times 10^{-3}$	$9.05(0.05) \times 10^{-3}$
13	$9.07(0.05) \times 10^{-3}$	$9.05(0.05) \times 10^{-3}$
14	$9.02(0.04) \times 10^{-3}$	$9.05(0.05) \times 10^{-3}$
15	$9.05(0.05) \times 10^{-3}$	$9.06(0.05) \times 10^{-3}$
16	$9.06(0.05) \times 10^{-3}$	$9.02(0.04) \times 10^{-3}$
17	$9.05(0.05) \times 10^{-3}$	$9.05(0.05) \times 10^{-3}$
18	$9.05(0.05) \times 10^{-3}$	$9.05(0.05) \times 10^{-3}$
19	$9.05(0.05) \times 10^{-3}$	$9.05(0.05) \times 10^{-3}$

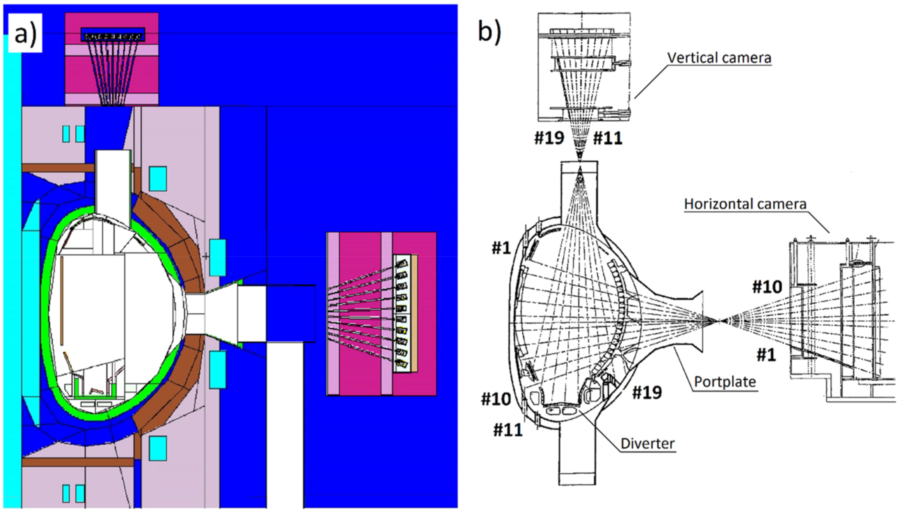

FIG. 10. MCNP JET model (a) and a poloidal cross section of the JET neutron camera, adapted from JG96.200-3c in the JET Figure Database,[22] copyright by EFDA-JET. Reproduced with permission from Hägg *et al.*, Rev. Sci. Instrum. **94**, 073502 (2023). Copyright 2023 AIP Publishing.

5. JET model

The JET model is used to simulate the backscatter neutron rate. A poloidal slice of the model is shown in Fig. 10 together with the schematic of the JET neutron camera for reference. For the MCNP settings used in the JET model, we simulate only neutrons and their elastic and inelastic scattering.

The backscatter neutrons are much more downshifted in energy compared to the in-scatter neutrons. The energy spectrum for the backscatter neutrons in channel 15 of this model is found in Fig. 11. Note that the spectrum will vary between detector channels.

MCNP simulations with the JET model provide a backscatter neutron spectrum in units of neutrons per the number of neutrons produced in the plasma. The spectrum is scaled with the estimated neutron yield, see Sec. III C, for a given neutron emissivity profile. The scaled backscatter neutron spectrum is then folded with the system response matrix to produce a light yield spectrum. Summing above the 6 MeVee light yield threshold yields the backscatter neutron count rate in each channel.

C. Neutron yield

Calculating the total neutron yield Y_n from a given neutron emissivity profile is performed by evaluating the emissivity on a poloidal grid, integrating toroidally over the entire torus, and then summing all grid values. We determine the neutron emissivity profile with the Gaussian model by performing a fit where we compare the simulated neutron rate m to the measured neutron rate λ in all channels. We use the center point coordinates (R_0, Z_0) and the standard deviations (σ_R, σ_Z) as model parameters. The scale factor r_n is set so that the sum of measured neutron counts in all channels equals the sum of simulated neutron counts in all channels. The model parameters are determined using a Markov chain Monte Carlo algorithm[33] and maximizing the sum of Poisson log likelihoods for

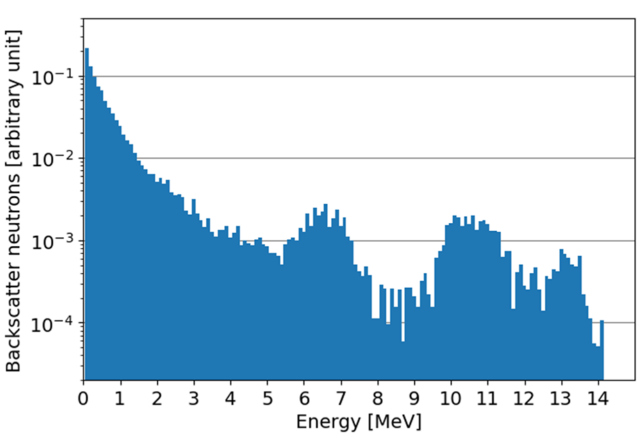

FIG. 11. An example of a neutron energy spectrum for backscattered neutrons in channel 15 in the MCNP JET model.

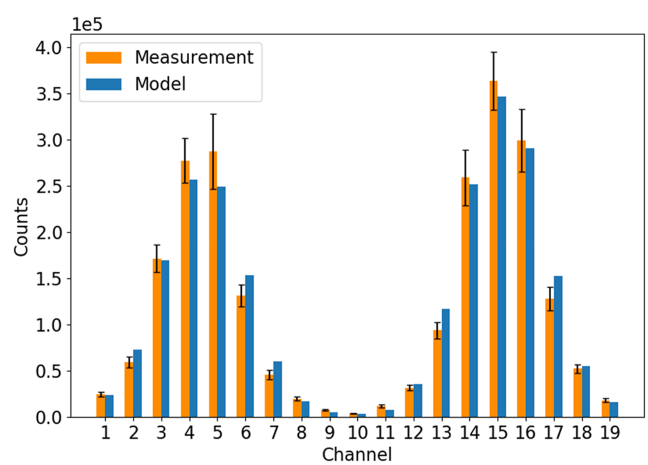

FIG. 12. Measured and modeled neutron count profile for JET shot 99950 in the time interval of 10.0–10.5 s.

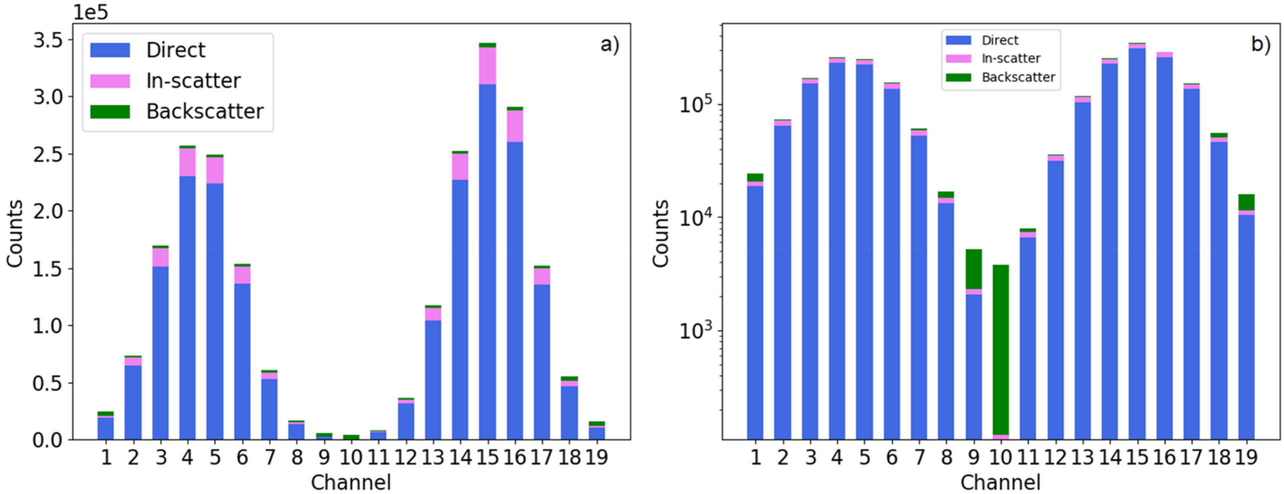

FIG. 13. Modeled neutron count profile for JET shot 99950 in the time interval 10.0–10.5 s. The profile is divided into the contributions from direct, in-scatter, and backscatter neutrons, shown in linear (a) and log (b) scale.

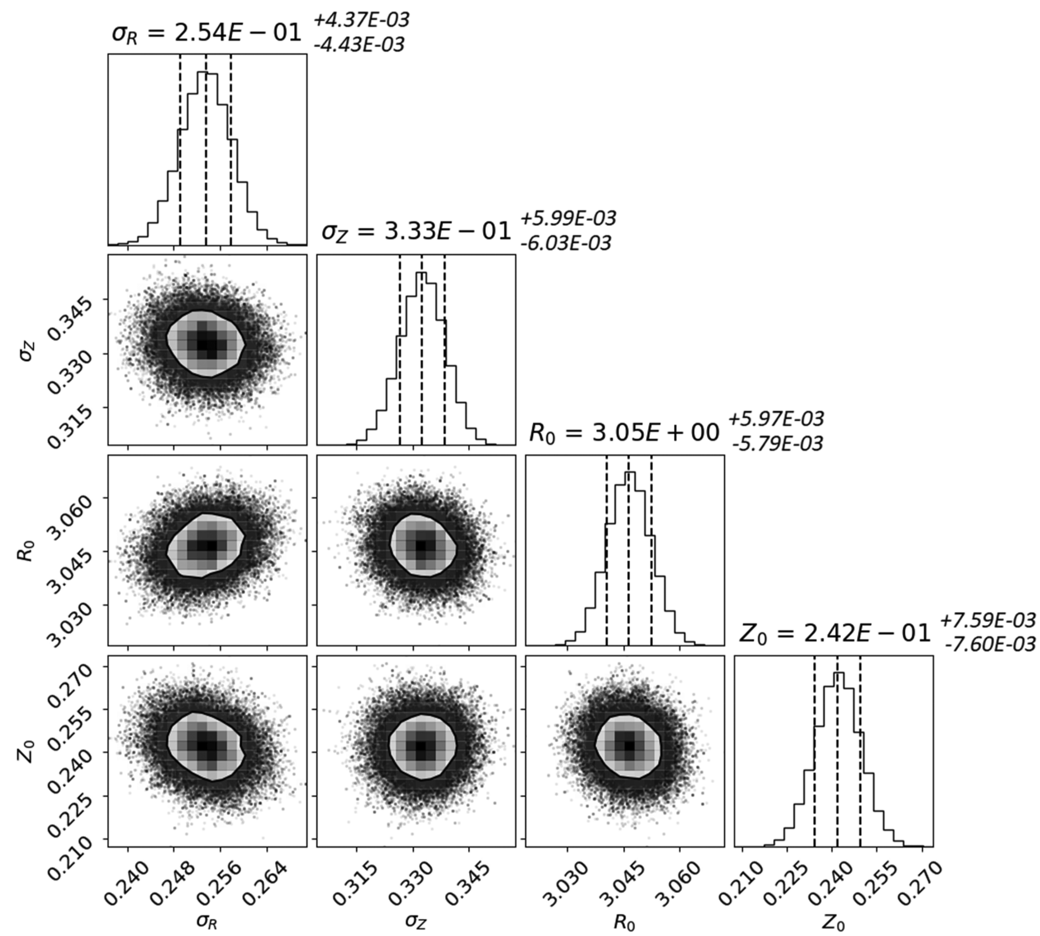

FIG. 14. Covariances between the parameters used in the Markov chain for JET shot 99950 in the time interval 10.0–10.5 s. The 1D histograms on top show the parameter values explored by the Markov chain. The dashed lines mark the 1-sigma uncertainty region for each parameter. The central values for each parameter, along with the 1-sigma uncertainties, are also printed above the 1-D histograms.

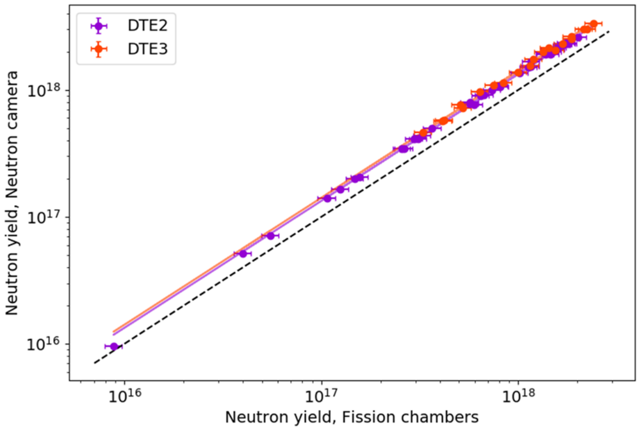

FIG. 15. Estimated neutron yield from the neutron camera vs the average neutron yield estimated by the fission chambers. The black dashed line has a slope of 1 and corresponds to a perfect agreement between the two. The purple and orange lines are fitted to the DTE2 and DTE3 datasets using orthogonal distance regression. Their slopes are 1.34 for DTE2 and 1.41 for DTE3. The uncertainties for the estimated neutron yield from the neutron camera are not visible in this figure due to the scale; they range between 1.9% and 4.9% and can be found in full in Appendix A. Note that the neutron camera uncertainties only contain statistical and calibration uncertainties; they do not contain any other systematic uncertainties (see Sec. V C 1).

all channels. The Poisson log likelihood for detector channel i is expressed as

$$L_i = \log \frac{\lambda_i^{m_i} e^{-\lambda_i}}{m_i!}, \tag{10}$$

where λ_i and m_i are the measured and simulated neutron rates above the light yield threshold. In each iteration of the Markov chain, the following steps are taken:

1. Calculate the simulated direct neutron rate and apply the efficiency factors.
2. Calculate the neutron yield for $r_n = 1$ [see Eq. (8)] and use it to scale the simulated backscatter neutron rate.
3. Sum the simulated direct and backscatter neutron rates.
4. Set r_n and calculate the log likelihood L.

An example of the number of measured and simulated neutrons detected in each channel is shown in Fig. 12. The contribution of direct, in-scatter, and backscatter neutrons is shown in Fig. 13. In this example, in-scatter neutrons contribute to around 8% of events. The backscatter component contributed to 1% of events in channel 4% and 13% of events in channel 8. Almost all events in channel 10 are due to backscatter.

The covariances between the model parameters sampled in the Markov chain, along with their central values and uncertainties, are displayed in a so-called corner plot in Fig. 14. The rows and columns of the figure each correspond to different parameters. The diagonal of the figure shows the one-dimensional steady state distribution of each model parameter from the Markov chain. The two-dimensional off-diagonal plots show the correlation between intersecting parameters. In large part, the model parameters are independent of one another, and the Markov chain converges comfortably. Note that the parameter uncertainties shown in Fig. 14 only reflect statistical uncertainties.

IV. RESULTS

A. Neutron yield estimates

The neutron yield has been estimated with the Gaussian model for 39 DTE2 shots and 20 DTE3 shots. These estimates are compared to neutron yield estimates from the JET fission chambers. The shot numbers, time intervals, neutron yield estimates, and fit parameter values are listed in Table XI, Appendix A. The level of agreement between the neutron camera and fission chamber estimates of the neutron yield is shown absolutely in Fig. 15 and as a ratio in Fig. 16.

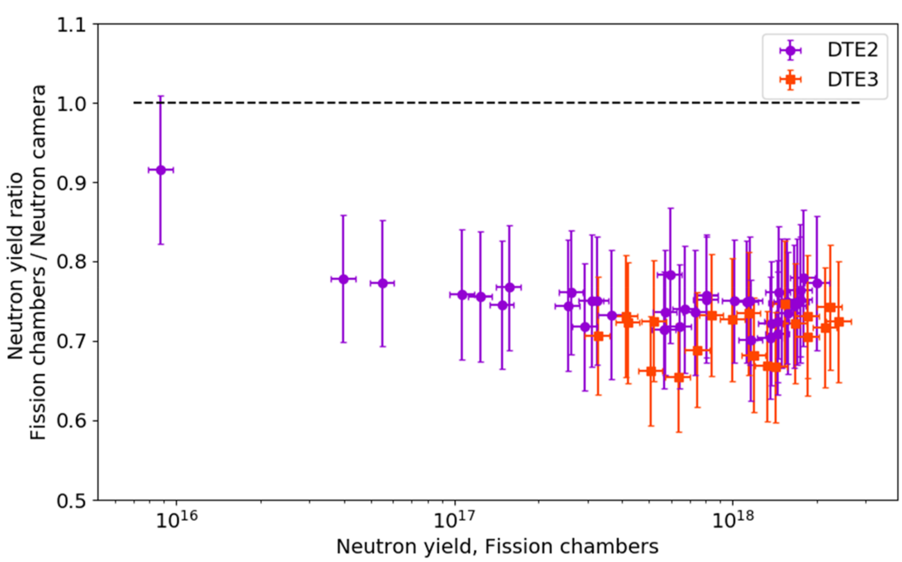

FIG. 16. Ratio between the fission chamber and camera neutron yield estimates vs the average neutron yield estimated by the fission chambers.

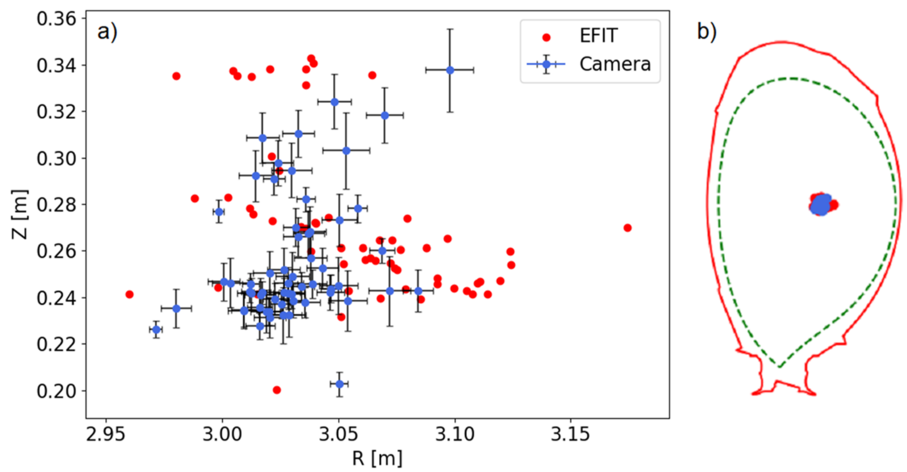

FIG. 17. (a) Spread of the neutron emission centers estimated by the neutron camera and the plasma center positions estimated by EFIT. The error bars mark the 1-sigma uncertainties for the estimated neutron emission centers. (b) Grouping of central positions shown in a poloidal slice of the torus.

A 10% uncertainty is assumed for the fission chamber estimates. The uncertainties for the neutron camera estimates are based on both the calibration uncertainties (see Sec. II A 2) and on the statistical uncertainties of the model parameters from the Markov chain. Between the shots analyzed in this work, the neutron yield uncertainties range from 1.9% to 4.9%, with an average of 3.5%.

Lines are fitted to the DTE2 and DTE3 datasets in Fig. 15 using orthogonal distance regression.[34] Their slopes are 1.34 for DTE2 and 1.41 for DTE3, meaning that the neutron camera on average estimates a 34% and 41% higher neutron yield than the fission chamber estimate for DTE2 and DTE3, respectively. A line fitted to all DTE2 and DTE3 points has the slope 1.36, meaning an overall estimate of 36% above the fission chamber estimate (this discrepancy is discussed further in Sec. V).

B. Plasma position

The Gaussian model also estimates the central position of the neutron emission, which is related to the central position of the plasma. This is compared to the fixed Gaussian model, which uses EFIT to find the central position, as opposed to letting R_0 and Z_0 be free parameters. The estimates from the fixed Gaussian model are listed in Table XII in Appendix A. The central position estimates from the Gaussian models and EFIT are shown in Fig. 17; the offsets between these two estimates are shown in Fig. 18. On average, the neutron emission central positions estimated by the neutron camera are shifted inwards in the torus compared to the EFIT estimates of the plasma center.

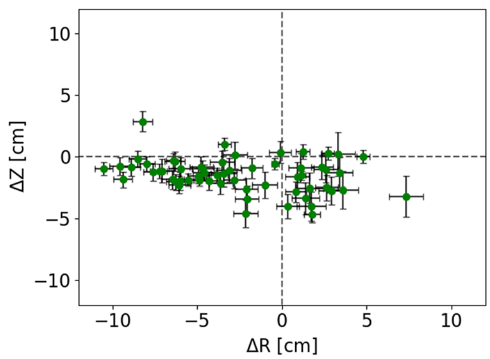

FIG. 18. Offset between the neutron emission centers estimated by the neutron camera and the plasma center positions estimated by EFIT. A negative ΔR indicates that the neutron emission center is positioned more inwards in the torus compared to the plasma center. A negative ΔZ indicates that the neutron emission center is positioned further down in the torus compared to the plasma center. The error bars mark the 1-sigma uncertainties for the offset positions, based on the estimated neutron emission centers.

V. DISCUSSION

This work describes an independent, first principle physics method for estimating the DT neutron yield using data from the JET neutron camera. This is a method for absolutely calibrating the neutron camera through measurement data and modeling, as opposed to a relative calibration to other neutron diagnostics. It is an adaptation of an earlier work[19] that estimated the DD neutron yield with a similar method. Several different models of the neutron camera have been used to account for in-scatter, backscatter, and transmission effects for the neutron emission from the plasma. The transmission through the rotatable steel collimators in particular is more important for DT neutrons compared to DD neutrons. A system response function is used to convert a neutron spectrum incident on a detector to a light yield spectrum simulating the detector measurement. This work estimates the neutron yield for a group of JET shots from the DTE2 and DTE3 campaigns in 2021 and 2023, respectively. The neutron camera measurements have been calibrated using large sums of thermal data from the two campaigns. The neutron yield estimates have been compared to estimates from the JET fission chambers.[17] On average, the neutron camera estimates higher neutron yields than the fission chambers (34% higher for DTE2 and 41% higher for DTE3). These discrepancies are relatively stable through the two campaigns, but in absolute terms the neutron yields determined with the two techniques are clearly inconsistent with each other. The reason for this discrepancy is presently unknown, but it is clear that the methodology presented in this paper is not without its flaws and approximations, as discussed in more detail below which, when addressed, could hopefully either narrow the gap between the two instruments or give further insight toward the actual neutron yield. The topics below are presented in no particular order.

A. High rates

For shots with higher neutron rates, pile-up makes up a significant portion of the measurement data. When processing the data, pile-up events are identified and corrected for using the assumption that both pile-up events and non-pile-up events originate from the same neutron energy distribution. The portion of pile-up events that fully overlap and appear as a single pulse is not identified by our method. This leads to some overestimation of higher energy events, which impacts the number of counts above our light yield threshold. The size of this contribution has not been estimated. For future work, the full pile-up contribution can be accounted for through modeling with techniques such as those described in Ref. 35. One could also utilize pile-up reconstruction algorithms such as Ref. 36 to reduce the impact of pile-up.

Shots with higher neutron rates may also impact the detector gain in the moment.[37] In a preliminary study, a shot with 61% pile-up was compared to a shot with 11% pile-up. The PHS of the higher pile-up rate shot is comparatively downshifted in light yield. This preliminary estimate suggests that the higher pile-up rate shot should have 7% more neutron counts above the light yield threshold if we were to correct for the gain shift. This implies that the DT neutron yield estimate with the neutron camera should be larger for higher rate shots, further widening the gap between it and the fission chamber estimate. This shift could greatly impact the neutron yield estimate, and future work should strongly consider implementing correction factors based on the observed shift at different neutron rates or using other methods to mitigate this effect.

B. Calibration

The light yield calibration of the neutron camera uses measurement data from shots heated solely by Ohmic heating, referred to as thermal data. Sums of thermal data from many shots are used to acquire a sufficient number of counts. An attempt was made to monitor the gain drift over DTE2 by calibrating five overlapping shot groups and performing a linear approximation. The large calibration uncertainties yielded vague results regarding the long term gain drift. For DTE3, a single shot group was used, which means the impact of gain drift is averaged over the campaign. In both cases, the large calibration uncertainties were propagated through the analysis into an uncertainty of the neutron yield estimate. The measured thermal spectra are fitted against modeled thermal spectra to determine the light yield calibration. The successful calibration fits indicate that the models describe the measurement data well, but one should still be aware of the potential points of failure in this calibration method. The modeled thermal spectrum relies on a model of the camera geometry and a light yield function by Adams[32] describing the plastic scintillators. The variation in light yield characteristics between the detectors is addressed in a secondary calibration, but the light yield function is still used as a base. Acquiring enough statistics from thermal data requires summing many hundreds of shots. As an alternative, the detector boxes are equipped with ^{22}Na sources used to calibrate the liquid scintillators in DD measurements. However, the low energies from ^{22}Na would require a hefty extrapolation to be used in calibrating DT measurements, and after an initial study, we chose not to pursue that path. Since the light yield calibration determines the position of the light yield threshold and, consequently, the number of counts in each detector channel, it can greatly impact the neutron yield estimate.

C. Models

The neutron emission profile has been modeled using a two-dimensional Gaussian with a variable central position. The neutron yield has been estimated by fitting the Gaussian model to neutron camera measurement data. As a preliminary sensitivity study of the Gaussian model, we also estimated the neutron yield using models of the neutron emission profile by the plasma transport code TRANSP.[12] When using the more advanced model from TRANSP for three different shots, the resulting neutron yields were within 6% of the Gaussian model estimates. This gives confidence that the Gaussian model is not overly simplified for performing these estimates.

Our method assumes a monoenergetic DT neutron emission from the plasma of 14 MeV. Furthermore, we assume an isotropic neutron emission from the plasma. In future work, these constraints can be lifted by utilizing DRESS.[38] With DRESS in combination with TRANSP, we can calculate the full neutron spectra incident at each detector based on the velocity distribution of the fuel ions, along with the pitch angle of neutron emission.

We have also compared the Gaussian model to a fixed Gaussian model, which uses a central position derived from the magnetic flux surfaces with EFIT.[30] Estimates of the central position for neutron emission and the plasma center reveal that while the two are close, they are not interchangeable in the Gaussian model. The difference between the two central positions was as large as 10 cm for some shots but typically around 5 cm. In most cases the neutron emission obtained from the Gaussian model is centered further inward in the torus than the plasma center calculated by EFIT. For the purpose of estimating the neutron yield, a central position shift of this magnitude is not an important factor. The neutron yield estimates from the fixed Gaussian model agree closely with those of the Gaussian model.

1. Systematic uncertainties

In the modeling of the neutron camera, it is assumed that the vertical camera has the same port attenuation as the horizontal camera. It is likely that there are some differences between the horizontal and vertical ports, but these have not been estimated in this work.

Due to the lack of up-to-date drawings of the JET neutron camera, there are systematic uncertainties regarding the camera position relative to the plasma. The information that has been found is conflicting and presents a possible 1 cm shift of the vertical neutron camera. This discrepancy has been investigated in this work by shifting the LINE2.1 model of the vertical camera 1 cm in the positive major radius direction. Performing the neutron yield estimate with the shifted geometry resulted in only a sub-percentage difference in the neutron yield from the non-shifted geometry. We therefore deem this particular geometric uncertainty to be insignificant.

There are also systematic uncertainties regarding the exact dimensions of the detector box and its contents. This has been modeled to the best of our abilities based on the illustration in

Appendix B, but any major discrepancies compared to the actual dimensions could heavily impact our results.

The simple model of the neutron emission profile also gives rise to a systematic uncertainty. As discussed earlier in the TRANSP comparison, this could introduce a shift as large as 6% of the neutron yield estimate.

D. Conclusion

The DT neutron yield has been estimated using the JET neutron camera for a selection of JET shots from the DTE2 and DTE3 campaigns. The results are not in agreement with corresponding neutron yield estimates from the JET fission chambers. The neutron camera estimates higher neutron yields compared to the fission chambers, on average 34% higher for DTE2 and 41% higher for DTE3. We are more inclined to believe the fission chamber results given their relatively straightforward calibration method. This work details the neutron camera method, its potential points of failure, and what improvements can be made.

ACKNOWLEDGMENTS

This work has been carried out within the framework of the EUROfusion Consortium, funded by the European Union via the Euratom Research and Training Program (Grant Agreement No. 101052200—EUROfusion). The views and opinions expressed are, however, those of the author(s) only and do not necessarily reflect those of the European Union or the European Commission. Neither the European Union nor the European Commission can be held responsible for them.

AUTHOR DECLARATIONS

Conflict of Interest

The authors have no conflicts to disclose.

Author Contributions

Linus Hägg: Conceptualization (equal); Data curation (lead); Formal analysis (lead); Investigation (lead); Methodology (equal); Project administration (lead); Software (lead); Supervision (equal); Validation (lead); Visualization (lead); Writing – original draft (lead); Writing – review & editing (lead). **Sean Conroy**: Conceptualization (equal); Formal analysis (supporting); Methodology (equal); Project administration (supporting); Software (equal); Writing – review & editing (equal). **Göran Ericsson**: Conceptualization (equal); Formal analysis (supporting); Funding acquisition (lead); Project administration (equal); Supervision (equal); Writing – review & editing (equal). **Zamir Ghani**: Data curation (equal); Resources (equal). **Luca Giacomelli**: Software (supporting). **Daniele Marocco**: Resources (supporting); Software (supporting). **Alberto Milocco**: Resources (supporting); Software (supporting). **Marco Riva**: Resources (supporting); Software (supporting). **Benjamin Vingren**: Software (supporting); Writing – review & editing (equal). **Gustav Robertson**: Software (supporting). **Jacob Eriksson**: Funding acquisition (equal); Writing – review & editing (equal). **Erik Andersson Sundén**: Conceptualization (equal); Formal analysis (supporting); Investigation (equal); Methodology (equal); Project administration (equal); Supervision (equal); Writing – review & editing (equal).

DATA AVAILABILITY

Raw data were generated at the JET large scale facility. Derived data supporting the findings of this study are available from the corresponding author upon reasonable request.

APPENDIX A: COMPLETE FIT RESULTS

Parameter values and neutron yield estimates with absolute statistical uncertainties from the Gaussian model fit and the fission chambers are provided in Table XI. The same results for the fixed Gaussian model fit are found in Table XII.

TABLE XI. Parameter values and neutron yield estimates with absolute statistical uncertainties from the Gaussian model fit and the fission chambers.

Shot	Time interval (s)	R_0 (m)	Z_0 (m)	σ_R (m)	σ_Z (m)	Y_n neutron camera	Y_n fission chambers
99440	48.9–49.4	3.05	0.27	0.27	0.38	$3.43(0.17) \times 10^{17}$	2.56×10^{17}
99448	47.4–47.9	2.98	0.24	0.26	0.33	$4.14(0.20) \times 10^{17}$	3.11×10^{17}
99449	47.8–48.3	3.02	0.23	0.27	0.34	$2.04(0.09) \times 10^{18}$	1.45×10^{18}
99452	47.9–48.4	3.03	0.23	0.28	0.36	$1.94(0.08) \times 10^{18}$	1.36×10^{18}
99455	47.7–48.2	3.02	0.23	0.28	0.36	$1.66(0.07) \times 10^{18}$	1.16×10^{18}
99460	48–48.5	3.05	0.30	0.33	0.48	$4.11(0.20) \times 10^{17}$	2.95×10^{17}
99479	49.5–50	3.10	0.34	0.33	0.46	$4.99(0.24) \times 10^{17}$	3.66×10^{17}
99487	50.5–51	3.04	0.26	0.29	0.40	$1.64(0.07) \times 10^{17}$	1.24×10^{17}
99490	47.8–48.3	3.03	0.23	0.30	0.44	$1.99(0.08) \times 10^{17}$	1.48×10^{17}
99492	56.5–57	3.08	0.24	0.27	0.37	$1.41(0.06) \times 10^{17}$	1.07×10^{17}
99510	46–46.5	3.04	0.27	0.29	0.43	$4.34(0.17) \times 10^{17}$	3.26×10^{17}
99512	50–50.5	3.07	0.32	0.32	0.44	$7.76(0.30) \times 10^{17}$	5.71×10^{17}
99513	49–49.5	3.05	0.32	0.30	0.43	$9.08(0.36) \times 10^{17}$	6.72×10^{17}

TABLE XI. (*Continued*.)

Shot	Time interval (s)	R_0 (m)	Z_0 (m)	σ_R (m)	σ_Z (m)	Y_n neutron camera	Y_n fission chambers
99523	49.5–50	3.03	0.31	0.30	0.42	$9.96(0.37) \times 10^{17}$	7.33×10^{17}
99541	47.7–48.2	3.02	0.23	0.28	0.36	$1.99(0.07) \times 10^{18}$	1.45×10^{18}
99544	47.6–48.1	3.01	0.23	0.29	0.38	$1.07(0.03) \times 10^{18}$	8.01×10^{17}
99633	47.8–48.3	3.02	0.24	0.28	0.36	$1.06(0.02) \times 10^{18}$	8.05×10^{17}
99634	47.6–48.1	3.01	0.24	0.28	0.37	$1.35(0.03) \times 10^{18}$	1.01×10^{18}
99639	47.6–48.1	3.01	0.25	0.28	0.37	$1.50(0.03) \times 10^{18}$	1.12×10^{18}
99716	53–53.5	3.00	0.28	0.27	0.38	$9.61(0.18) \times 10^{15}$	8.79×10^{15}
99776	48.5–49	2.97	0.23	0.24	0.33	$7.13(0.16) \times 10^{16}$	5.51×10^{16}
99785	51–51.5	3.04	0.28	0.29	0.39	$5.13(0.12) \times 10^{16}$	3.99×10^{16}
99801	49–49.5	3.06	0.28	0.29	0.39	$3.45(0.08) \times 10^{17}$	2.63×10^{17}
99805	48.5–49	3.02	0.29	0.31	0.45	$7.93(0.19) \times 10^{17}$	5.67×10^{17}
99809	52.5–53	3.05	0.20	0.28	0.38	$2.04(0.04) \times 10^{17}$	1.57×10^{17}
99866	47.9–48.4	3.03	0.24	0.28	0.36	$2.15(0.06) \times 10^{18}$	1.58×10^{18}
99870	47.7–48.2	3.02	0.23	0.27	0.35	$2.23(0.07) \times 10^{18}$	1.66×10^{18}
99886	47.9–48.4	3.02	0.24	0.28	0.35	$2.08(0.07) \times 10^{18}$	1.56×10^{18}
99887	49.5–50	3.05	0.24	0.26	0.33	$2.33(0.08) \times 10^{18}$	1.75×10^{18}
99909	47.9–48.4	3.03	0.24	0.27	0.35	$2.27(0.08) \times 10^{18}$	1.70×10^{18}
99916	49.6–50.1	3.02	0.30	0.29	0.41	$1.54(0.06) \times 10^{18}$	1.16×10^{18}
99941	48.5–49	3.03	0.29	0.30	0.44	$8.96(0.38) \times 10^{17}$	6.43×10^{17}
99943	49.5–50	3.01	0.29	0.29	0.42	$1.90(0.08) \times 10^{18}$	1.37×10^{18}
99946	46.5–47	3.04	0.27	0.27	0.39	$7.59(0.32) \times 10^{17}$	5.94×10^{17}
99948	49.6–50.1	3.02	0.31	0.28	0.39	$2.00(0.09) \times 10^{18}$	1.50×10^{18}
99950	50–50.5	3.05	0.24	0.25	0.33	$2.30(0.10) \times 10^{18}$	1.75×10^{18}
99960	47.7–48.2	3.00	0.25	0.29	0.39	$1.92(0.08) \times 10^{18}$	1.46×10^{18}
99965	48.5–49	3.03	0.25	0.27	0.37	$2.61(0.12) \times 10^{18}$	2.01×10^{18}
99969	49.1–49.6	3.02	0.25	0.27	0.36	$2.30(0.10) \times 10^{18}$	1.79×10^{18}
104140	46.3–46.8	3.03	0.27	0.30	0.42	$7.66(0.23) \times 10^{17}$	5.08×10^{17}
104148	48.5–49	3.07	0.26	0.27	0.33	$9.74(0.30) \times 10^{17}$	6.37×10^{17}
104215	47.5–48	3.03	0.24	0.29	0.37	$2.14(0.06) \times 10^{18}$	1.43×10^{18}
104216	47.7–48.2	3.03	0.24	0.29	0.37	$2.00(0.06) \times 10^{18}$	1.34×10^{18}
104333	51.2–51.7	3.04	0.25	0.32	0.43	$1.09(0.03) \times 10^{18}$	7.48×10^{17}
104406	48–48.5	3.03	0.27	0.28	0.38	$1.75(0.06) \times 10^{18}$	1.19×10^{18}
104413	51.4–51.9	3.07	0.24	0.38	0.51	$4.63(0.16) \times 10^{17}$	3.27×10^{17}
104469	50.8–51.3	3.05	0.24	0.35	0.49	$5.82(0.19) \times 10^{17}$	4.21×10^{17}
104473	52–52.5	3.05	0.24	0.34	0.47	$5.66(0.19) \times 10^{17}$	4.14×10^{17}
104518	47.5–48	3.02	0.24	0.31	0.39	$2.64(0.08) \times 10^{18}$	1.86×10^{18}
104520	48–48.5	3.03	0.24	0.30	0.38	$3.00(0.10) \times 10^{18}$	2.15×10^{18}
104521	47.5–48	3.01	0.24	0.30	0.38	$2.32(0.07) \times 10^{18}$	1.68×10^{18}
104522	50–50.5	3.04	0.25	0.27	0.35	$3.33(0.11) \times 10^{18}$	2.41×10^{18}
104523	48.6–49.1	3.04	0.24	0.28	0.37	$2.54(0.08) \times 10^{18}$	1.86×10^{18}
104551	47.7–48.2	3.01	0.23	0.31	0.39	$1.56(0.05) \times 10^{18}$	1.14×10^{18}
104575	49–49.5	3.02	0.23	0.26	0.36	$1.37(0.05) \times 10^{18}$	9.99×10^{17}
104594	53–53.5	3.03	0.25	0.32	0.47	$7.21(0.23) \times 10^{17}$	5.22×10^{17}
104602	51.7–52.2	3.00	0.25	0.30	0.42	$1.15(0.04) \times 10^{18}$	8.39×10^{17}
104675	48.5–49	3.03	0.24	0.28	0.37	$3.01(0.10) \times 10^{18}$	2.23×10^{18}
104676	47.8–48.3	3.03	0.25	0.29	0.38	$2.07(0.07) \times 10^{18}$	1.55×10^{18}

TABLE XII. Parameter values and neutron yield estimates with absolute statistical uncertainties from the fixed Gaussian model fit and the fission chambers.

Shot	Time interval (s)	R_0 EFIT (m)	Z_0 EFIT (m)	σ_R (m)	σ_Z (m)	Y_n neutron camera	Y_n fission chambers
99440	48.9–49.4	3.02	0.30	0.26	0.39	$3.40(0.12)\times10^{17}$	2.56×10^{17}
99448	47.4–47.9	3.00	0.24	0.26	0.33	$4.15(0.14)\times10^{17}$	3.11×10^{17}
99449	47.8–48.3	3.07	0.24	0.27	0.34	$2.06(0.07)\times10^{18}$	1.45×10^{18}
99452	47.9–48.4	3.10	0.24	0.27	0.35	$1.96(0.07)\times10^{18}$	1.36×10^{18}
99455	47.7–48.2	3.08	0.24	0.27	0.35	$1.68(0.06)\times10^{18}$	1.16×10^{18}
99460	48–48.5	2.98	0.34	0.29	0.50	$4.01(0.13)\times10^{17}$	2.95×10^{17}
99479	49.5–50	3.06	0.34	0.32	0.46	$4.94(0.13)\times10^{17}$	3.66×10^{17}
99487	50.5–51	3.07	0.26	0.29	0.40	$1.65(0.05)\times10^{17}$	1.24×10^{17}
99490	47.8–48.3	3.02	0.24	0.30	0.44	$1.98(0.05)\times10^{17}$	1.48×10^{17}
99492	56.5–57	3.09	0.24	0.27	0.37	$1.41(0.03)\times10^{17}$	1.07×10^{17}
99510	46–46.5	3.01	0.28	0.28	0.44	$4.30(0.11)\times10^{17}$	3.26×10^{17}
99512	50–50.5	3.04	0.33	0.31	0.44	$7.68(0.18)\times10^{17}$	5.71×10^{17}
99513	49–49.5	3.04	0.34	0.30	0.44	$9.05(0.23)\times10^{17}$	6.72×10^{17}
99523	49.5–50	3.01	0.34	0.29	0.43	$9.87(0.25)\times10^{17}$	7.33×10^{17}
99541	47.7–48.2	3.09	0.25	0.27	0.35	$2.02(0.05)\times10^{18}$	1.45×10^{18}
99544	47.6–48.1	3.05	0.25	0.29	0.38	$1.07(0.02)\times10^{18}$	8.01×10^{17}
99633	47.8–48.3	3.05	0.23	0.28	0.35	$1.07(0.02)\times10^{18}$	8.05×10^{17}
99634	47.6–48.1	3.06	0.26	0.28	0.36	$1.36(0.02)\times10^{18}$	1.01×10^{18}
99639	47.6–48.1	3.07	0.26	0.28	0.36	$1.51(0.03)\times10^{18}$	1.12×10^{18}
99716	53–53.5	3.00	0.28	0.27	0.39	$9.61(0.12)\times10^{15}$	8.79×10^{15}
99776	48.5–49	2.96	0.24	0.23	0.33	$7.10(0.12)\times10^{16}$	5.51×10^{16}
99785	51–51.5	2.99	0.28	0.27	0.39	$5.07(0.07)\times10^{16}$	3.99×10^{16}
99801	49–49.5	3.05	0.27	0.29	0.39	$3.44(0.05)\times10^{17}$	2.63×10^{17}
99805	48.5–49	3.00	0.34	0.29	0.46	$7.87(0.13)\times10^{17}$	5.67×10^{17}
99809	52.5–53	3.02	0.20	0.27	0.39	$2.03(0.03)\times10^{17}$	1.57×10^{17}
99866	47.9–48.4	3.11	0.24	0.26	0.35	$2.18(0.05)\times10^{18}$	1.58×10^{18}
99870	47.7–48.2	3.09	0.25	0.26	0.34	$2.26(0.05)\times10^{18}$	1.66×10^{18}
99886	47.9–48.4	3.11	0.24	0.26	0.34	$2.12(0.05)\times10^{18}$	1.56×10^{18}
99887	49.5–50	3.11	0.25	0.25	0.32	$2.35(0.06)\times10^{18}$	1.75×10^{18}
99909	47.9–48.4	3.12	0.25	0.25	0.34	$2.31(0.07)\times10^{18}$	1.70×10^{18}
99916	49.6–50.1	3.02	0.34	0.28	0.42	$1.53(0.04)\times10^{18}$	1.16×10^{18}
99941	48.5–49	3.01	0.33	0.29	0.45	$8.88(0.27)\times10^{17}$	6.43×10^{17}
99943	49.5–50	3.04	0.34	0.29	0.43	$1.90(0.06)\times10^{18}$	1.37×10^{18}
99946	46.5–47	3.01	0.28	0.26	0.39	$7.55(0.21)\times10^{17}$	5.94×10^{17}
99948	49.6–50.1	3.04	0.34	0.28	0.40	$2.00(0.06)\times10^{18}$	1.50×10^{18}
99950	50–50.5	3.11	0.25	0.25	0.32	$2.32(0.08)\times10^{18}$	1.75×10^{18}
99960	47.7–48.2	3.04	0.26	0.29	0.39	$1.93(0.06)\times10^{18}$	1.46×10^{18}
99965	48.5–49	3.06	0.26	0.27	0.36	$2.62(0.09)\times10^{18}$	2.01×10^{18}
99969	49.1–49.6	3.05	0.26	0.27	0.36	$2.31(0.08)\times10^{18}$	1.79×10^{18}
104140	46.3–46.8	3.02	0.29	0.29	0.44	$7.63(0.14)\times10^{17}$	5.08×10^{17}
104148	48.5–49	3.17	0.27	0.25	0.32	$9.82(0.28)\times10^{17}$	6.37×10^{17}
104215	47.5–48	3.10	0.27	0.29	0.37	$2.15(0.04)\times10^{18}$	1.43×10^{18}
104216	47.7–48.2	3.12	0.26	0.28	0.36	$2.01(0.05)\times10^{18}$	1.34×10^{18}
104333	51.2–51.7	3.08	0.27	0.32	0.44	$1.10(0.02)\times10^{18}$	7.48×10^{17}
104406	48–48.5	3.11	0.24	0.28	0.36	$1.77(0.04)\times10^{18}$	1.19×10^{18}
104413	51.4–51.9	3.04	0.27	0.36	0.52	$4.57(0.09)\times10^{17}$	3.27×10^{17}
104469	50.8–51.3	3.04	0.27	0.34	0.50	$5.79(0.11)\times10^{17}$	4.21×10^{17}
104473	52–52.5	3.03	0.27	0.33	0.48	$5.63(0.11)\times10^{17}$	4.14×10^{17}
104518	47.5–48	3.08	0.26	0.31	0.39	$2.66(0.06)\times10^{18}$	1.86×10^{18}

TABLE XII. (*Continued*.)

Shot	Time interval (s)	R_0 EFIT (m)	Z_0 EFIT (m)	σ_R (m)	σ_Z (m)	Y_n neutron camera	Y_n fission chambers
104520	48–48.5	3.08	0.25	0.30	0.38	$3.02(0.06) \times 10^{18}$	2.15×10^{18}
104521	47.5–48	3.07	0.26	0.30	0.38	$2.34(0.05) \times 10^{18}$	1.68×10^{18}
104522	50–50.5	3.09	0.26	0.28	0.35	$3.35(0.07) \times 10^{18}$	2.41×10^{18}
104523	48.6–49.1	3.06	0.26	0.29	0.37	$2.55(0.05) \times 10^{18}$	1.86×10^{18}
104551	47.7–48.2	3.07	0.25	0.31	0.39	$1.57(0.03) \times 10^{18}$	1.14×10^{18}
104575	49–49.5	3.05	0.24	0.27	0.35	$1.38(0.03) \times 10^{18}$	9.99×10^{17}
104594	53–53.5	3.04	0.27	0.32	0.48	$7.22(0.14) \times 10^{17}$	5.22×10^{17}
104602	51.7–52.2	3.02	0.27	0.30	0.43	$1.15(0.02) \times 10^{18}$	8.39×10^{17}
104675	48.5–49	3.07	0.25	0.29	0.37	$3.03(0.06) \times 10^{18}$	2.23×10^{18}
104676	47.8–48.3	3.12	0.25	0.27	0.37	$2.08(0.05) \times 10^{18}$	1.55×10^{18}

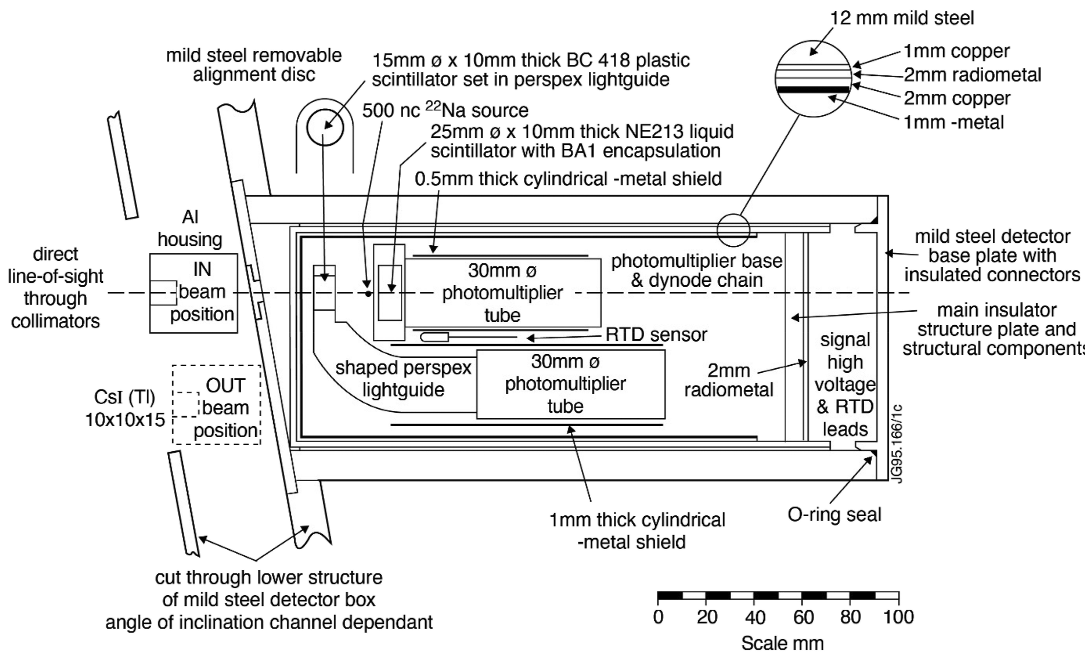

FIG. 19. Illustration of a detector box interior and its immediate surroundings. Reference number JG95.166-1c in the JET Figure Database,[22] copyright by EFDA-JET.

APPENDIX B: DETECTOR BOX ILLUSTRATION

Illustration of a detector box in the neutron camera (see Fig. 19).

REFERENCES

[1] J. Garcia, "Deuterium-tritium experiments in JET with the ITER-like wall," in TTF 2022–US-EU Joint Transport Taskforce Workshop, Santa Rosa, CA, April 2022.

[2] Eurofusion, "Breaking new ground: JET tokamak's latest fusion energy record shows mastery of fusion processes," available at https://euro-fusion.org/eurofusion-news/dte3record/, 2024.

[3] C. Hellesen, M. Albergante, E. A. Sundén, L. Ballabio, S. Conroy, G. Ericsson, M. G. Johnsson, L. Giacomelli, G. Gorini, A. Hjalmarsson, I. Jenkins, J. Källne, E. Ronchi, H. Sjöstrand, M. Tardocchi, I. Voitsekhovitch, M. Weiszflog, and JET-EFDA Contributors, "Neutron spectroscopy measurements and modeling of neutral beam heating fast ion dynamics," Plasma Phys. Controlled Fusion **52**, 085013 (2010).

[4] J. Eriksson, M. Nocente, F. Binda, C. Cazzaniga, S. Conroy, G. Ericsson, L. Giacomelli, G. Gorini, C. Hellesen, T. Hellsten, A. Hjalmarsson, A. S. Jacobsen, T. Johnson, V. Kiptily, T. Koskela, M. Mantsinen, M. Salewski, M. Schneider, S. Sharapov, M. Skiba, M. Tardocchi, M. Weiszflog, and JET Contributors, "Dual sightline measurements of MeV range deuterons with neutron and gamma-ray spectroscopy at JET," Nucl. Fusion **55**, 123026 (2015).

[5] M. Salewski, M. Nocente, A. S. Jacobsen, F. Binda, C. Cazzaniga, G. Ericsson, J. Eriksson, G. Gorini, C. Hellesen, A. Hjalmarsson, V. G. Kiptily, T. Koskela,

S. B. Korsholm, T. Kurki-Suonio, F. Leipold, J. Madsen, D. Moseev, S. K. Nielsen, J. Rasmussen, M. Schneider, S. E. Sharapov, M. Stejner, M. Tardocchi, and JET Contributors, "MeV-range velocity-space tomography from gamma-ray and neutron emission spectrometry measurements at JET," Nucl. Fusion **57**, 056001 (2017).

[6]O. N. Jarvis, "Neutron measurement techniques for tokamak plasmas," Plasma Phys. Controlled Fusion **36**, 209 (1994).

[7]B. Esposito, F. B. Marcus, J. M. Adams, S. Conroy, O. N. Jarvis, M. J. Loughlin, G. Sadler, P. v. Belle, and N. Watkins, "Ohmic ion temperature and thermal diffusivity profiles from the JET neutron emission profile monitor," Plasma Phys. Controlled Fusion **35**, 1433–1440 (1993).

[8]C. Hellesen, J. Eriksson, F. Binda, S. Conroy, G. Ericsson, A. Hjalmarsson, M. Skiba, M. Weiszflog, and JET-EFDA Contributors, "Fuel ion ratio determination in NBI heated deuterium tritium fusion plasmas at JET using neutron emission spectrometry," Nucl. Fusion **55**, 023005 (2015).

[9]J. Eriksson, G. Castegnetti, S. Conroy, G. Ericsson, L. Giacomelli, C. Hellesen, and JET-EFDA Contributors, "Deuterium density profile determination at JET using a neutron camera and a neutron spectrometer," Rev. Sci. Instrum. **85**, 11E106 (2014).

[10]G. Ericsson, S. Conroy, M. Gatu Johnson, E. Andersson Sundén, M. Cecconello, J. Eriksson, C. Hellesen, S. Sangaroon, M. Weiszflog, and JET EFDA Contributors, "Neutron spectroscopy as a fuel ion ratio diagnostic: Lessons from JET and prospects for ITER," Rev. Sci. Instrum. **81**, 10D324 (2010).

[11]G. Bonheure, S. Popovichev, L. Bertalot, A. Murari, S. Conroy, J. Mlynar, I. Voitsekhovitch, and JET-EFDA Contributors, "Neutron profiles and fuel ratio n_T/n_D measurements in JET ELMy H-mode plasmas with tritium puff," Nucl. Fusion **46**, 725–740 (2006).

[12]C. Hellesen, E. A. Sundén, S. Conroy, G. Ericsson, L. Giacomelli, A. Hjalmarsson, M. G. Johnsson, J. Källne, E. Ronchi, M. Weiszflog, L. Ballabio, G. Gorini, M. Tardocchi, I. Voitsekhovitch, and JET-EFDA Contributors, "Validating TRANSP simulations using neutron emission spectroscopy with dual sight lines," Rev. Sci. Instrum. **79**, 10E510 (2008).

[13]C. Hellesen, E. Andersson Sundén, S. Conroy, G. Ericsson, J. Eriksson, M. Gatu Johnson, M. Weiszflog, and JET-EFDA Contributors, "Neutron spectroscopy results of JET high-performance plasmas and extrapolations to DT performance," Rev. Sci. Instrum. **81**, 10D337 (2010).

[14]F. Binda, G. Ericsson, J. Eriksson, C. Hellesen, S. Conroy, E. A. Sundén, and JET EFDA Contributors, "Forward fitting of experimental data from a NE213 neutron detector installed with the magnetic proton recoil upgraded spectrometer at JET," Rev. Sci. Instrum. **85**, 11E123 (2014).

[15]J. M. Adams, O. N. Jarvis, G. J. Sadler, D. B. Syme, and N. Watkins, "The JET neutron emission profile monitor," Nucl. Instrum. Methods Phys. Res., Sect. A **329**, 277–290 (1993).

[16]O. N. Jarvis, J. M. Adams, F. B. Marcus, and G. J. Sadler, "Neutron profile measurements in the Joint European Torus," Fusion Eng. Des. **34–35**, 59–66 (1997).

[17]D. B. Syme, S. Popovichev, S. Conroy, I. Lengar, L. Snoj, and JET EFDA Contributors, "Fusion yield measurements on JET and their calibration," Nucl. Eng. Des. **246**, 185–190 (2012).

[18]P. Batistoni, S. Popovichev, Z. Ghani, A. Cufar, L. Giacomelli, P. Hawkins, K. Keogh, S. Jednorog, E. Laszynska, S. Loreti *et al.*, "14 MeV calibration of JET neutron detectors—Phase 2: In-vessel calibration," Nucl. Fusion **58**, 106016 (2018).

[19]L. Hägg, F. Binda, S. Conroy, G. Ericsson, Z. Ghani, L. Giacomelli, D. Marocco, A. Milocco, M. Riva, and E. Andersson Sundén, JET Contributors, "Estimating the neutron yield in a deuterium plasma with the JET neutron camera," Rev. Sci. Instrum. **94**, 073502 (2023).

[20]Luxium Solutions, "Solid plastic scintillators," available at https://luxium-solutions.com/radiation-detection-scintillators/plastic-scintillators/fast-timing-bc-418-bc-420-bc-422-bc-422q, 2024.

[21]G. F. Knoll, *Radiation Detection and Measurement* (John Wiley and Sons, Inc., 2000).

[22]The EUROfusion internal Figure Database, available at https://figures.jetdata.eu, 2022.

[23]F. Binda, J. Eriksson, G. Ericsson, C. Hellesen, S. Conroy, M. Nocente, E. Andersson Sundén, and JET Contributors, "Generation of the neutron response function of an NE213 scintillator for fusion applications," Nucl. Instrum. Methods Phys. Res., Sect. A **866**, 222–229 (2017).

[24]K. H. Behringer *et al.*, "Impurity and radiation studies during the JET Ohmic Heating Phase," Nucl. Fusion **26**(6), 751 (1986).

[25]P. Van Belle and G. Sadler, "The computation of fusion product spectra from high temperature plasmas," in *Proceedings of the Course Workshop on Basic and Advanced Techniques for Fusion Plasmas*, 3 (Commission Of The European Communities and Monotypia Franchi, Varenna, 1986), p. 767.

[26]L. Ballabio, J. Källne, and G. Gorini, "Relativistic calculation of fusion product spectra for thermonuclear plasmas," Nucl. Fusion **38**, 1723 (1998).

[27]W. Cash, "Parameter estimation in astronomy through application of the likelihood ratio," Astrophys. J. **228**, 939–947 (1979).

[28]A. Sahlberg *et al.*, "Spatially resolved measurements of RF accelerated deuterons at JET," Nucl. Fusion **61**, 036025 (2021).

[29]E. Ronchi, S. Conroy, E. A. Sundén, G. Ericsson, M. G. Johnson, C. Hellesen, H. Sjöstrand, and M. Weiszflog, "A parametric model for fusion neutron emissivity tomography for the KN3 neutron camera at JET," Nucl. Fusion **50**, 035008 (2010).

[30]L. C. Appel, G. T. A. Huysmans, L. L. Lao, P. J. McCarthy, D. G. Muir, E. R. Solano, J. Storrs, D. Taylor, and W. Zwingmann, "A unified approach to equilibrium reconstruction," in *2006 33rd EPS Conference on Plasma Physics* (European Physical Society, Rome, 2006), p. P2.184.

[31]F. Binda, G. Ericsson, S. Conroy, and E. Andersson Sundén, "Calculation of the profile-dependent neutron backscatter matrix for the JET neutron camera system," Fusion Eng. Des. **123**, 865–868 (2017).

[32]S. Conroy, private communication (2023).

[33]D. Foreman Mackey, D. W. Hogg, D. Lang, and J. Goodman, "emcee: The MCMC hammer," Publ. Astron. Soc. Pac. **125**(925), 306 (2013).

[34]P. T. Boggs and J. E. Rogers, "Orthogonal distance regression," in *Statistical Analysis of Measurement Error Models and Applications: Proceedings of the AMS-IMS-SIAM Joint Summer Research Conference Held June 10–16, 1989* (American Mathematical Society, 1990), p. 186.

[35]A. Sahlberg *et al.*, "Forward modeling of pile-up events in liquid scintillator detectors for neutron emission spectroscopy," Rev. Sci. Instrum. **92**, 083502 (2021).

[36]M. Preston, S. Bukreeva, S. Diehl, P. Marciniewski, R. W. Novotny, S. Ryzhikov, P. A. Semenov, and P.-E. Tegnér, "A feature-extraction and pile-up reconstruction algorithm for the forward-spectrometer EMC of the PANDA experiment," Nucl. Instrum. Methods Phys. Res., Sect. A **1011**, 165601 (2021).

[37]A. K. Gupta and N. Nath, "Gain stability in high-current photomultipliers at high variable counting rates," Nucl. Instrum. Methods **53**, 352–354 (1967).

[38]J. Eriksson, S. Conroy, E. Andersson Sundén, and C. Hellesen, "Calculating fusion neutron energy spectra from arbitrary reactant distributions," Comput. Phys. Commun. **199**, 40–46 (2016).